Studies on intracellular protein-protein interactions using bioluminescence resonance energy transfer

佐々木, 理

https://doi.org/10.15017/1806835

出版情報：九州大学, 2016, 博士（理学）, 課程博士
バージョン：

Studies on intracellular protein-protein interactions using bioluminescence resonance energy transfer

Osamu Sasaki

Graduate School of Systems Life Sciences,

Kyushu University, Fukuoka, Japan

2016

CONTENTS

Page

PART1

A structural perspective of the MAVS-regulatory mechanism on the mitochondrial outer membrane using bioluminescence resonance energy transfer

ABBREVIATIONS

BiFC; bimolecular fluorescence complementation

BRET; bioluminescence resonance energy transfer

CARD; caspase activation and recruitment domain

HCV; hepatitis C virus

HEK; human embryonic kidney

IFN-β; interferon β

IRF-3; interferon regulatory factor 3

MAVS; mitochondrial antiviral signaling

Mfns; mitofusins

NF-κB; nuclear factor κB

NLRX1; NOD-like receptor family member X1

PRR; proline rich region

RIG-I; retinoic acid-inducible gene I

Rluc; *Renilla* luciferase

RLR; RIG-I-like receptor

Venus; a yellow fluorescent protein derivative

SUMMARY

In most eukaryotic cells, mitochondria have various essential roles for proper cell function, such as energy production, and in mammal mitochondria also act as a platform for antiviral innate immunity. Mitochondrial mediated antiviral immunity depends on the activation of the cytoplasmic retinoic acid-inducible gene I (RIG-I)-like receptors (RLRs) signaling pathway, and on the participation of mitochondrial antiviral signaling (MAVS), which is localized on the mitochondrial outer membrane. After RNA virus infection, RLRs translocate to the mitochondrial surface to interact with MAVS, and the adaptor protein undergoes a conformational change that is essential for downstream signaling, although its structural features are poorly understood. Here we examined the MAVS-regulatory mechanism on the mitochondrial outer membrane using bioluminescence resonance energy transfer (BRET) in live cells. Using a combination of BRET and functional analysis, we found that the activated MAVS conformation is a highly ordered oligomer, at least more than three molecules per complex unit on the membrane. Hepatitis C virus NS3/4A protease and mitofusin 2, which are known MAVS inhibitors, interfere with MAVS homotypic oligomerization in a distinct manner, each differentially altering the active conformation of MAVS. Our results reveal structural features underlying the precise regulation of MAVS signaling on the mitochondrial outer membrane, and may provide insight into other signaling systems involving organelles.

INTRODUCTION

RNA viruses gain entry into host cells either through endocytosis, where the plasma membrane engulfs the virion, resulting in the release of the virion constituents into the cell, or through membrane fusion with the plasma membrane, resulting in the immediate release of viral replication machinery and incorporation of the corresponding nucleic acids into the host cytoplasm. To counter the plasma membrane fusion of RNA viruses, vertebrates have evolved the retinoic acid-inducible gene I (RIG-I)-like receptors (RLRs) pathway, which detects cytoplasmic viral-derived double-stranded (ds)RNA and induces a signaling cascade to initiate an antiviral innate immune response (1,2). In humans, the RLRs pathway detects several viruses from five families (Paramyxoviridae, Orthomyxoviridae, Rhabdoviridae, Flaviviridae, and Reoviridae), which include hepatitis C, Dengue, Japanese encephalitis, rabies, and influenza A viruses (3,4).

The initial sensors of intracellular viral RNA are caspase activation and recruitment domain (CARD)-containing RNA-helicase proteins, RIG-I and melanoma differentiation-associated gene 5 (MDA5), which differ based on the size and type of the viral RNA (3–5). Post-nucleotide recognition by the RLRs (6,7) leads to translocation of the RNA helicases to the scaffold adaptor protein, mitochondrial antiviral signaling (MAVS (8); also known as IPS-1 (9), VISA (10), and Cardif (11)), a ubiquitously expressed mitochondrial outer membrane protein. Upon the upstream signaling event, MAVS is proposed to undergo a conformational switch that leads to the recruitment of various

downstream effectors, such as tumor necrosis factor receptor-associated factor (TRAF) family members and tumor necrosis factor receptor-associated death domain (TRADD), to form a supramolecular signaling assembly. The mitochondrial hub of the protein complex, the so-called MAVS signalosome, is essential for upregulation of the transcriptional factors nuclear factor κB (NF-κB) and interferon regulatory factor-3 (IRF-3), leading to the rapid production of type I interferons (IFNs) and proinflammatory cytokines (12,13).

Because the prominent function of MAVS signaling is precisely regulated upon viral infection (13–15), it is crucial to understand how the conformational switch is regulated and the machinery involved in activating and inactivating MAVS signaling. In fact, these processes comprise transiently populated states during the signaling event, making it difficult to directly determine the structure of MAVS. Further, MAVS signaling occurs on the mitochondrial surface, so it is somewhat altered when reconstituted under isolated in vitro conditions. In the present study, we bypassed the practical issues mentioned above and investigated the MAVS-regulatory mechanism in live cells using a fluorescence-based assay combined with functional study. Our results indicated that MAVS undergoes a homotypic interaction, resulting in a highly oligomerized state toward signaling. The hepatitis C virus (HCV) protease NS3/4A, NOD-like receptor family member X1 (NLRX1), and mitofusin 2 (Mfn2), all of which are known MAVS inhibitors (12,13,15), differentially target the

MAVS conformation to inhibit its actions. Based on these findings, we provide structural insight into mitochondrial-mediated antiviral signaling.

EXPERIMENTAL PROCEDURES

Materials and cell cultures – The human embryonic kidney (HEK) 293 cell line was maintained in Dulbecco's modified Eagle medium (D-MEM; GIBCO BRL, Carlsbad, CA) supplemented with 1% L-glutamine, 1% penicillin–streptomycin, and 10% bovine calf serum (BCS) at 5% CO 2 and 37 °C. The rabbit polyclonal antibody against human MAVS was described previously (16). Anti-Myc (9E10) and anti-HA (HA.11) monoclonal antibodies were purchased from Covance (Princeton, NJ), anti-phospho-IRF-3 (Ser396) rabbit monoclonal (4D4G), anti-Hsp60, and anti-COX IV polyclonal (D307) antibodies were obtained from Cell Signaling Technology (Danvers, MA), and anti-mtHsp70 monoclonal antibody was purchased from Affinity BioReagents (Golden, CO). Anti-β-actin, anti-Mfn2, and anti-Tom-20 monoclonal antibodies, as well as anti-Mfn1 and anti-cytochrome c polyclonal antibodies, were obtained from Santa Cruz Biotechnology (Santa Cruz, CA), anti-GFP antibody was from MBL (Nagoya, Japan), and anti-OPA-1 monoclonal antibody was from BD Biosciences (San Jose, CA). Coelenterazine H was purchased from Promega (Madison, WI). The NLRX1-deficient mouse embryonic fibroblast (MEF) was kindly provided by Jenny Ting (University of North Carolina at Chapel Hill). All other reagents were of biochemical research grade.

Plasmid construction and mutagenesis – Polymerase chain reaction (PCR) was performed with PrimeSTAR DNA polymerase (Takara, Tokyo, Japan). Fusion-tagged MAVS-expression

plasmids were constructed by ligating the PCR amplimer into a pcDNA3.1 (−) vector (Invitrogen, Carlsbad, CA) that encoded either an N-terminal Venus or Rluc tag. Mutation (C508R) into Venus- or Rluc-MAVS plasmids was introduced by site-directed mutagenesis (Stratagene, La Jolla, CA). The Myc-tagged versions of MAVS, Mfn1, Mfn2, and their variants were described previously (16). The NLRX1 variants were created by amplifying the regions comprising amino acids 1–975 (full length), 40–975 (mature), and 40–560 (NACHT) by using PCR, and ligating the PCR products into the pcDNA3.1 (−) vector that encoded either an N-terminal or C-terminal HA-tag. To generate retroviral expression constructs of NLRX1 variants, each HA-tagged NLRX1 cDNA was recloned into the retroviral vector pMXs-Puro (Cell Biolabs, San Diego, CA). The retroviral expression vectors were then transfected into the platinum packaging cell lines (Cell Biolabs), and the retroviral supernatant was harvested 48 h post-transfection and used to infect MEF cultures. All constructs used in the present study were confirmed by DNA sequencing (ABI 3100).

Dual luciferase reporter assay – Luciferase assays were performed as described previously (17) with a slight modification. In brief, HEK293 cells were plated in 24-well plates (2×10^5 cells/well). The following day, the cells were co-transfected with 50 ng of a luciferase reporter plasmid (p125luc, pELAM, or pISRE-Luc), 2.5 ng of Renilla luciferase internal control vector phRL-TK (Promega), and each of the indicated vectors using Lipofectamine 2000 reagent (Invitrogen). An empty vector [pcDNA3.1 (−)] was used to maintain equivalent amounts of DNA in each well. Cells were harvested

24 h post-transfection and analyzed by a dual-luciferase reporter assay on the GloMax 20/20n luminometer (Promega).

BRET saturation assay – All the BRET signals were measured using a Flexstation 3 Microplate Reader (Molecular Devices, Sunnyvale, CA) at 37 °C. For the assay, HEK293 cells were plated in 12-well plates (2.5×10^5 cells/well). The following day, the cells were co-transfected with a constant quantity (5 ng) of Rluc-tagged plasmid and increasing amounts of Venus-tagged constructs using Lipofectamine 2000. Empty vector [pcDNA3.1 (−)] was also used to maintain equivalent amounts of DNA in each well. Twenty hours post-transfection, the cells were washed once with 1× phosphate-buffered saline (PBS, pH 7.2), mechanically detached, and collected by centrifugation (800 g for 5 min). The cell pellets were then resuspended in 80 µL of Dulbecco's PBS (pH 7.2), and two 40-µL aliquots of cell suspensions were transferred to each well of white 96-well microplates (duplicate wells). After adding 10 µL of Rluc substrate (coelenterazine H, 25 µM) into each sample, followed by 30 s of gentle mixing, luminescence was measured simultaneously for the donor (λ_{em} =475 nm; short wavelength) and for the acceptor (λ_{em} =530 nm; long wavelength). Saturation data analysis was performed using the following equation, described previously (18):

BRET signal = [long wavelength] /[short wavelength]− [long wavelength] $_{donor\ only}$ /[short wavelength]$_{donor\ only}$:

Mitochondrial fractionation and proteolysis – HEK293 cells were washed once with cold PBS (pH 7.2), scraped off the culture plate, and lysed in 800 μL homogenization buffer [20 mM HEPES (pH 7.5), 70 mM sucrose, and 220 mM mannitol] by 30 strokes in a Dounce homogenizer. The homogenate was centrifuged at 800 g for 5 min, and the resulting supernatant was further centrifuged at 11,000 g for 10 min (4 °C) to precipitate the crude mitochondrial fraction. After washing the pellet once with the homogenization buffer, the isolated mitochondrial fraction was resuspended into homogenization buffer and treated with trypsin (100 μg/mL) in the absence or presence of 0.05% (w/v) digitonin. The proteolytic reaction was performed on ice for 15 min, and the reactants were subjected to Western blot analysis with the indicated antibodies.

Electron microscopy (EM) – For EM, cells were processed as previously described (19). In brief, the cells were pre-fixed in 1× PBS containing 2% formaldehyde and 2% glutaraldehyde for 1 h, washed twice with 1× PBS, and post-fixed with 1% osmium solution at 4 °C. Cells were then washed, stained with 0.5% aqueous uranyl acetate for 1 h, dehydrated through a graded series of ethanol, and embedded in Epon. Sections (70 nm) were cut on an EM UC6 ultramicrotome (Leica, Wetzlar, Germany), stained with 2% uranyl acetate in 70% ethanol and Reynolds' lead citrate, and analyzed on a JEOL JEM-1010 EM at 80 kV. Images were recorded with an Olympus Soft Imaging System VELETA CCD camera. For morphometry, at least 200 mitochondria from individual cells were scored in total.

Confocal microscopy – NLRX1$^{-/-}$ MEFs were plated on coverslips in 12-well plates (4 × 10^4 cells/well). The next day, the cells were infected with the retroviral supernatants. Forty-eight hours post-infection, cells were fixed with 3.7% formaldehyde for 10 min, permeabilized with 0.1% Triton X-100 in 1× PBS (pH 7.2), and blocked with 5% BCS. The expressed HA-tagged NLRX1 constructs were detected with antibody against HA (HA.11) and Alexa Fluor 488-conjugated secondary antibody, and mitochondria were visualized by mitochondrial-targeted red fluorescent protein. Cells were imaged by a Carl Zeiss LSM510 confocal microscope.

Results

Validation of bioluminescence resonance energy transfer (BRET) constructs − BRET is a powerful tool for evaluating protein–protein interactions in live cells. Because it does not require an external excitation source, which often results in photobleaching, BRET provides a comparable range of biological macromolecular complexes (≤10 nm) [18]. To elucidate the structural characteristics of MAVS signaling on the mitochondrial outer membrane, we first designed two variants of human MAVS, containing either Venus- or Rluc-fusion tags at their N-termini (denoted as Venus-MAVS and Rluc-MAVS, respectively). Functionally, the Venus-MAVS construct was almost identical to the original MAVS protein we used previously [16], and it potently activated both IFN-β and NF-κB reporter plasmids in a dose-dependent manner (Fig. 1A). Consistent with the reporter assay, the overexpression of Venus-MAVS in HEK293 cells promoted endogenous IRF-3 phosphorylation (second panel, Fig. 1B), a hallmark of IRF-3 activation. However, co-expression of NS3/4A (an inhibitor of the RLRs pathway), a serine protease that cleaves MAVS from the mitochondrial membrane, impaired the activation of both IRF-3 and NF-κB (far right lanes, Fig. 1A, B), as previously reported [11,20]. Similarly, the behavior of the Rluc-MAVS construct was almost identical to that of the Venus-MAVS (Supplementary Fig. S1). We therefore concluded that the addition of either fusion tag (approximately 27- or 35-kDa proteins) to MAVS had no effect on its overall function in signal transduction.

MAVS homo-oligomerization involved in antiviral signal transduction − We analyzed the structural characteristics of the MAVS-activated conformation using a BRET-based assay in live cells. The interaction between Venus-MAVS and Rluc-MAVS was successfully monitored using a BRET saturation assay (filled squares, Fig. 1C), which displayed a hyperbolic saturation curve characteristic of the specific interaction [18], although neither the interaction between Rluc protein and Venus-MAVS nor that between the fusion proteins (Rluc/Venus) themselves were observed (Supplementary Fig. S2). To confirm that our observed MAVS–MAVS interaction was not a result of nonspecific interactions and/or aggregation on the mitochondrial membrane, we next tested the Venus-tagged versions of two mitochondrial outer membrane proteins (Tom-22 and Omp-25) instead of Venus-MAVS, and these proteins were co-transfected with Rluc-MAVS. Increasing the amounts of either Venus-Tom-22 or Venus-Omp-25 did not increase the strength of BRET signals (open triangles or circles, Fig. 1C). We mapped the region of this homotypic interaction via the C-terminal region of MAVS (cross symbols, Fig. 1D), which includes the single spanning transmembrane region (see Supplementary Fig. S3). These results suggest that anchoring on the mitochondrial outer membrane would be relevant to both function and protein–protein interaction (Fig. 1D, E, and Supplementary Fig. S4). To verify that the observed MAVS–MAVS interaction in live cells would also form even highly ordered oligomers as previously reported [21], we sought a complementation assay (bimolecular fluorescence complementation; BiFC) combined with the BRET system (Supplementary

Fig. S5). Neither the N-terminal truncated version of Venus [Venus(C)] nor its C-terminal truncated [Venus(N)] proteins fused with MAVS produced a positive fluorescent signal (left images, Fig. 2A). However, co-expression of both constructs [Venus(N+C)-MAVS] absolutely complemented the signal in a dose-dependent manner (green squares in the right panel, Fig. 2A), indicating that homotypic MAVS interactions, as seen above, caused the functional reconstitution. Most importantly, a positive BiFC BRET saturation curve was observed between the complemented Venus pair of the proteins and Rluc-MAVS (green squares, Fig. 2B), demonstrating that the activated MAVS conformation is a highly ordered oligomer, as we expected of at least more than three molecules on the outer membrane (Supplementary Fig. S5B). We hypothesized that this conformational change in MAVS molecules might be due to a drastic membrane dynamics arrangement, because the ultrastructure of the mitochondrial intermembrane space expanded (arrowheads in the right panel, Fig. 2C) when the Sendai virus (SeV), a negative-stranded RNA virus of the Paramyxoviridae family, was infected into their host cells [the vast majority of mitochondria show an abnormal ultrastructure (~89%) when cells are challenged by SeV infection (Supplementary Fig. S6)].

NS3/4A abolishes MAVS–MAVS interactions − Studies of the conformational changes in MAVS involved in the signaling allowed us to explore MAVS in a quiescent state by negative regulators. We first examined the effect of the HCV NS3/4A, which cleaves MAVS at its cysteine residue at amino acid position 508 [11,20] (left panel, Fig. 3A). Our MAVS constructs were also

inactivated by proteolytic cleavage, as observed in previous studies (far right lanes, Fig. 1A, B). In preliminary tests of our BRET assay, we introduced a C508R substitution into Venus-MAVS and Rluc-MAVS constructs resistant to proteolysis attack by NS3/4A [20] (right panel, Fig. 3A). The C508R variants activated both IRF-3 and NF-κB in a dose-dependent manner (Fig. 3B, C), indicating that they were functionally indistinguishable from their wild-type counterparts, except that they were resistant to NS3/4A attack (far right lane, Fig. 3C).

Consistent with the results of the functional assay, a specific interaction between the MAVS mutants was observed in the BRET saturation assay (green triangles, Fig. 3D), and the saturation profile was unaffected even when NS3/4A was co-expressed (yellow triangles, Fig. 3D). In contrast, the BRET saturation profile of the wild-type counterparts was impaired when they were co-expressed with NS3/4A (red squares, Fig. 3D), due to the cleavage of MAVS (Fig. 1B). These results are consistent with the fact that the cytosolic-distributed MAVS mutants (amino acids 1–514) abolished homotypic MAVS interactions (opened circles, Fig. 1D). Moreover, our BRET results are also supported by the findings of *Lamarre* and colleagues, who reported that an HCV protease inhibitor did not disrupt the MAVS interaction even when co-expressed with NS3/4A, as monitored by their BRET system [22].

BRET saturation assay in the presence of other MAVS inhibitors − Mitochondrial proteins NLRX1 and Mfn2 are reported to play inhibitory roles in the RLRs pathway (16,23–25). However, whether or not these inhibitors affect MAVS–MAVS interaction is unclear. We next investigated how NLRX1 and Mfn2 affect MAVS interaction by monitoring their effects via BRET, which is sensitive to miniscule changes in protein conformation.

NOD-like receptor family member X1 (NLRX1) − HEK293 cells were co-transfected with the BRET pairs of MAVS constructs (Venus- and Rluc-) with the NLRX1 plasmid. We observed fine hyperbolic saturated curves, reflecting the homotypic MAVS–MAVS interactions, even in the presence of exogenous NLRX1 (red circles, Fig. 4A). To examine the submitochondrial localization of the expressed NLRX1, isolated mitochondria from the cells were treated with trypsin in the absence or presence of digitonin. We confirmed that NLRX1 was resistant to tryptic digestion even in the presence of digitonin, which similarly behaved as a matrix protein (mtHsp70), whereas the treatment drastically degraded outer membrane (MAVS, Mfn1, Mfn2, and Tom20) or intermembrane (Cyt c) space proteins (Fig. 4B). The results of this assay implied that the vast majority of NLRX1 was translocated to the mitochondrial matrix, as previously reported [26], further supporting the observation that the NLRX1 expression did not affect the structural rearrangement of cytosol-faced MAVS oligomerization (Fig. 4A). An interesting structural feature of NLRX1 is that it possesses an N-terminal addressing sequence that is essential for mitochondrial targeting [26,27]. When we masked

the addressing sequence by attaching an N-terminal hemagglutinin tag (N-term) or deleting its signal sequence (first 39 amino acids) (mature), we found that the expression of these variants affected the MAVS–MAVS interaction (interfered with the MAVS association), which was detected via BRET saturation assay (blue squares and red triangles, Fig. 4C). However, the BRET signal of the C-terminal HA version of NLRX1 protein behaved similarly to that of the intact protein (yellow circles, Fig. 4C and Supplementary Fig. S7), suggesting that the subcellular localization of the mitochondrial protein ultimately affected the MAVS–MAVS interaction (Fig. 4C, D). We confirmed that the observed BRET data on MAVS–MAVS interaction with the truncated NLRX1 was not attributable to a nonspecific jamming of the TOM/TIM machinery, because other controls that normally target the mitochondrial matrix (Tfam) or inner membrane (O.S. and T.K., unpublished data) and its mutants lacking part of the mitochondrial addressing sequences exhibited fine hyperbolic saturated curves (Supplementary Fig. S8).

Mitofusin 2 (Mfn2) − On the other hand, integral mitochondrial outer membrane protein Mfn2 differentially targeted the MAVS–MAVS interaction and decreased the BRET signal (red squares, Fig. 5A), confirming that abundant Mfn2 rearranged MAVS oligomerization in a dose-dependent manner (Supplementary Fig. S9). Having identified that Mfn2 affected MAVS homotypic interactions, we performed structure-function analyses to define the Mfn2 region responsible for this modulation. Three dissected fragments of Mfn2 (GTPase, 4,3 hydrophobic heptad repeat region 1

[HR1], and HR2 regions; see Supplementary Fig. S10) were tested for their ability to interfere with MAVS oligomerization. Of these fragments, the middle region of Mfn2 (Mfn2/HR1) was capable of creating a BRET saturation curve similar to that of the full-length molecule (yellow triangles, Fig. 5B). As expected, the functional role of the HR1 region correlated with our BRET data, and we confirmed that abundant Mfn2/HR1 suppressed IRF-3 activation (right panel, Fig. 5B), as we previously observed via reporter assay [16]. In addition, overexpression of the Mfn2/HR1 fragment in HEK293 cells potently and dose-dependently interfered with the complementation of the Venus fluorescence signal by prohibiting MAVS–MAVS interactions (Fig. 5C), thereby decreasing the BiFC BRET signal (Fig. 5D). Taken together, these results indicate that Mfn2 modulates MAVS inactivation on the mitochondrial outer membrane through its HR1 region.

Discussion

During the activation of MAVS, a scaffold protein on the outer mitochondrial membrane, various downstream effectors are recruited to form a signaling supramolecular assembly that ultimately leads to the upregulation of NF-κB and IRF-3 (1,2,4,13). Despite the many efforts to identify adaptor molecules that interact with MAVS, it remains poorly understood how the scaffold protein undergoes its multi-step structural transition between inactive to active conformations. In the present study, we used a BRET-based assay to evaluate the MAVS-regulatory mechanism in live cells, which is in a transient state on the mitochondrial outer membrane.

Activation of MAVS molecules – On the basis of fluorescence assays, two other groups previously reported that MAVS dimerization is essential for downstream signal transduction of the RLRs pathway (22,28). In particular, Wang and colleague reported that the formation of MAVS homodimers leads MAVS activation and to bind to a downstream molecule, TRAF3 (28). Our results agree with their assumption that MAVS homotypic oligomerization is involved in MAVS signaling, although we strongly believe that the activated conformation of MAVS is much more highly oligomerized than they detected, containing at least more than three molecules in the complex unit (Figs. 2 and 6A). Consistent with our observation, a recent crystal structure analysis revealed that the trimeric form of TRAF3 recognizes equal stoichiometric composition of MAVS molecules (29),

implying a post-MAVS activation state. Interestingly, Chen's group provided evidence in an in vitro study that viral infection induces the formation of prion-like MAVS aggregates (21), which would be predicted to be much a larger mass than our observed oligomers. However, on the basis of our results together with these assumptions, it is likely that MAVS homotypic oligomerization, namely the protein concentration on the mitochondrial membrane foci, is an essential step in the activation of MAVS signaling. These oligomer formations of the scaffold protein are presumably essential for downstream signaling in another system, because the stimulator of interferon genes (STING), an ER-integrated membrane protein involved in anti-cytosolic DNA innate immunity (30), is reported to be formed in a homo-oligomeric state in response to stimulation (31).

We propose that the MAVS concentration step (post-RLRs binding to MAVS) is not only triggered by local foci on the mitochondrial surface, but also by some dynamic rearrangement of membrane composition (such as inner membrane and/or intermembrane space), which affects molecular collision via an integrated transmembrane domain (red arrows, Fig. 6A). In fact, the present study shows dynamic expansion of the intermembrane space in virus-infected cells (Fig. 2C), and we and others reported that disrupting the mitochondrial membrane potential, an essential physiologic function of mitochondria, perturbs MAVS-mediated antiviral signaling (17,32). At present, we cannot exclude the possibility that some cytosolic factors chaperone MAVS–MAVS associations post-RLRs

translocation to MAVS, but there is no doubt that MAVS functions are interconnected with membrane potency (17).

Negative regulation of MAVS – Our results indicate that NS3/4A, NLRX1, and Mfn2, which are inhibitors of the RLRs pathway, differentially affect MAVS (Fig. 6B). First, NS3/4A is categorized as a target cleavage group, and once this protein is expressed in the cytosol of the host cell, it proteolytically inhibits MAVS function. Mislocalization of MAVS from the mitochondrial membrane leads to improper unfolding of the protein, resulting in diminished oligomerization (top model, Fig. 6B), and the idea is also supported by the finding that deleting the TM domain in mutant MAVS abolishes its self-association (Fig. 1D). Although our BRET system failed to distinguish whether this protease targeted pre- or post-MAVS activation, we were able to monitor the severe disruption of the BRET signal (see Fig. 3D). Another type of MAVS inhibitor, 3ABC, a cysteine protease from hepatitis A (33), is also in this category. NLRX1 localizes predominantly to the mitochondrial matrix (26,27) and is also reported to be present on the outer membrane (23), but how it inhibits MAVS-signaling is unclear. Consistent with the results of Arnoult and colleagues (26), we confirmed that NLRX1 existed predominantly in the matrix, and our BRET results revealed that overexpression of NLRX1 did not interfere with the MAVS conformation (Fig. 4A, C). This is likely due to the fact that NLRX1 does not produce a steric constraint when it localizes at the mitochondrial matrix side. Therefore, the most likely explanation for its mechanism is that NLRX1 bypasses other factors existing in the mitochondria,

and together they engage in the negative regulation of MAVS (middle model, Fig. 6B). Recently, Ting and colleagues reported that the mitochondrial Tu translation elongation factor (TUFM) links the NLRX1 and RLRs pathways (25), and this might be an excellent candidate. On the other hand, the expression of either the mature form or the masking of its mitochondrial targeting sequence using an epitope tag of NLRX1 proteins did not support this idea. Although NLRX1 would be translocated predominantly to the mitochondrial matrix, we cannot exclude the possibility that a small portion of cytosol-retained NLRX1 acts as our observed phenotype, such as a mature-form protein in the physiologic condition, and inhibits MAVS signaling (Fig. 4C, D). This possibility also suggests how gC1qR (also known as p32 (34)) is involved in the down regulation of the RLRs pathway (35) (it should be noted that its actual localization is controversial).

Finally, the mitochondrial outer membrane protein Mfn2 interacts with MAVS through its HR1 region, and we propose that it stably sequesters MAVS on the outer mitochondrial membrane by diluting the highly homogeneous MAVS concentration to a more heterogeneous population, resulting in a disruption of apparent MAVS–MAVS interactions (bottom model, Fig. 6B). To strengthen our model, we monitored different migrations of MAVS-containing fractions by size exclusion chromatography when the endogenous Mfn2 level was knocked down (16). In the present study, we observed that Mfn2 dose-dependently deducted the BRET intensity of MAVS oligomerization. Thus, we believe that Mfn2 would prevent a homogeneous MAVS concentration state by steric hindrance.

In conclusion, the MAVS conformational changes upon its regulation on the mitochondrial membrane are transient during its antiviral signal transduction, making the direct determination of its structural elements difficult. In the present study, BRET analysis provided important insight into the structural features of MAVS and may lead to an advanced approach to signal transduction studies.

REFERENCES

1. T. Kawai, S. Akira, Innate immune recognition of viral infection, Nat. Immunol. 7(2006) 131–137.

2. O. Takeuchi, S. Akira, Innate immunity to virus infection, Immunol. Rev. 227(2009) 75–86.

3. H. Kato, O. Takeuchi, S. Sato, M. Yoneyama, M. Yamamoto, K. Matsui, S. Uematsu,A. Jung, T .Kawai, K.J. Ishii, O. Yamaguchi, K. Otsu, T. Tsujimura, C.S. Koh, C. Reis eSousa, Y. Matsuura, T. Fujita, S. Akira, Differential roles of MDA5 and RIG-Ihelicases in the recognition of RNA viruses, Nature 441 (2006) 101–105.

4. M. Yoneyama, T. Fujita, RNA recognition and signal transduction by RIG-I-like receptors, Immunol. Rev. 227 (2009) 54–65.

5. H. Kato, O. Takeuchi, E. Mikamo-Satoh, R. Hirai, T. Kawai, K. Matsushita, A. Hiiragi,T.S. Dermody, T. Fujita, S. Akira, Length-dependent recognition of double-stranded ribonucleic acids by retinoic acid-inducible gene-I and melanoma differentiation-associated gene 5, J. Exp. Med. 205 (2008) 1601–1610.

6. E. Kowalinski, T. Lunardi, A.A. McCarthy, J. Louber, J. Brunel, B. Grigorov, D. Gerlier, S. Cusack, Structural basis for the activation of innate immune pattern-recognition receptor RIG-I by viral RNA, Cell 147 (2011) 423–435.

7. D. Luo, S.C. Ding, A. Vela, A. Kohlway, B.D. Lindenbach, A.M. Pyle, Structural in-

sights into RNA recognition by RIG-I, Cell 147 (2011) 409–422.

8. R.B. Seth, L. Sun, C.K. Ea, Z.J. Chen, Identification and characterization of MAVS, a mitochondrial antiviral signaling protein that activates NF-κB and IRF-3, Cell 122 (2005) 669–682.

9. T. Kawai, K. Takahashi, S. Sato, C. Coban, H. Kumar, H. Kato, K.J. Ishii, O. Takeuchi, S. Akira, IPS-1, an adaptor triggering RIG-I- and Mda5-mediated type I interferon induction, Nat. Immunol. 6 (2005) 981–988.

10. L.G. Xu, Y.Y. Wang, K.J. Han, L.Y. Li, Z. Zhai, H.B. Shu, VISA is an adapter protein required for virus-triggered IFN-β signaling, Mol. Cell 19 (2005) 727–740.

11. E. Meylan, J. Curran, K. Hofmann, D. Moradpour, M. Binder, R. Bartenschlarger, J.Tschopp, Cardif is an adaptor protein in the RIG-I antiviral pathway and is targeted by hepatitis C virus, Nature 437 (2005) 1167–1172.

12. S.M. Belgnaoui, S. Paz, J. Hiscott, Orchestrating the interferon antiviral response through the mitochondrial antiviral signaling (MAVS) adapter, Curr. Opin.Immunol. 23 (2011) 564–572.

13. A.P. West, G.S. Shadel, S. Ghosh, Mitochondria in innate immune responses, Nat.Rev. Immunol. 11 (2011) 389–402.

14. D. Arnoult, F. Soares, I. Tattoli, S.E. Girardin, Mitochondria in innate immunity,EMBO Rep. 12 (2011) 901–910.

15. T. Koshiba, Mitochondrial-mediated antiviral immunity, Biochim. Biophys. Acta1833 (2013) 225–232.

16. K. Yasukawa, H. Oshiumi, M. Takeda, N. Ishihara, Y. Yanagi, T. Seya, S. Kawabata, T.Koshiba, Mitofusin 2 inhibits mitochondrial antiviral signaling, Sci. Signal. 2 (2009) ra47.

17. T. Koshiba, K. Yasukawa, Y. Yanagi, S. Kawabata, Mitochondrial membrane poten-tial is required for MAVS-mediated antiviral signaling, Sci. Signal. 4 (2011) ra7.

18. K.D. Pfleger, K.A. Eidne, Illuminating insights into protein–protein interactions using bioluminescence resonance energy transfer (BRET), Nat. Methods 3 (2006) 165–174.

19. T. Koshiba, S.A. Detmer, J.T. Kaiser, H. Chen, J.M. McCaffery, D.C. Chan, Structural basis of mitochondrial tethering by mitofusin complexes, Science 305 (2004) 858–862.

20. X.D. Li, L. Sun, R.B. Seth, G. Pineda, Z.J. Chen, Hepatitis C virus protease NS3/4Acleaves mitochondrial antiviral signaling protein off the mitochondria to evadeinnate immunity, Proc. Natl. Acad. Sci. U. S. A. 102 (2005) 17717–17722.

21. F. Hou, L. Sun, H. Zheng, B. Skaug, Q.X. Jiang, Z.J. Chen, MAVS forms functionalprion-like aggregates to activate and propagate antiviral innate immune response, Cell 146 (2011) 448–461.

22. M. Baril, M.E. Racine, F. Penin, D. Lamarre, MAVS dimer is a crucial signaling component of innate immunity and the target of hepatitis C virus NS3/4A protease, J. Virol. 83 (2009) 1299–1311.

23. C.B. Moore, D.T. Bergstralh, J.A. Duncan, Y. Lei, T.E. Morrison, A.G. Zimmermann,M.A. Accavitti-Loper, V.J. Madden, L. Sun, Z. Ye, J.D. Lich, M.T. Heise, Z. Chen, J.P.Ting, NLRX1 is a regulator of mitochondrial antiviral immunity, Nature 451(2008) 573–577.

24. I.C. Allen, C.B. Moore, M. Schneider, Y. Lei, B.K. Davis, M.A. Scull, D. Gris, K.E.Roney, A.G. Zimmermann, J.B. Bowzard, P. Ranjan, K.M. Monroe, R.J. Pickles, S.Sambhara, J.P. Ting, NLRX1protein attenuates inflammatory responses to infection by interfering with the RIG-I-MAVS and TRAF6-NF-κB signaling pathways, Immunity 34 (2011) 854–865.

25. Y. Lei, H. Wen, Y. Yu, D.J. Taxman, L. Zhang, D.G. Widman, K.V. Swanson, K.W. Wen, B.Damania, C.B. Moore, P.M. Giguère, D.P. Siderovski, J. Hiscott, B. Razani,C.F. Semenkovich, X. Chen, J.P. Ting, The mitochondrial proteins NLRX1 and TUFM form a complex that regulates type I interferon and autophagy, Immunity36 (2012) 933–946.

26. D. Arnoult, F. Soares, I. Tattoli, C. Castanier, D.J. Philpott, S.E. Girardin, An N-terminal addressing sequence targets NLRX1 to the mitochondrial matrix, J. Cell Sci. 122 (2009) 3161–3168.

27. I. Tattoli, L.A. Carneiro, M. Jéhanno, J.G. Magalhaes, Y. Shu, D.J. Philpott, D. Arnoult,S.E. Girardin, NLRX1 is a mitochondrial NOD-like receptor that amplifies NF-κB and JNK pathways by inducing reactive oxygen species production, EMBO Rep.9 (2008) 293–300.

28. E.D. Tang, C.Y. Wang, MAVS self-association mediates antiviral innate immune signaling, J. Virol. 83 (2009) 3420–3428.

29. P. Zhang, A. Reichardt, H. Liang, R. Aliyari, D. Cheng, Y. Wang, F. Xu, G. Cheng, Y. Liu, Single amino acid substitutions confer the antiviral activity of the TRAF3adaptor protein onto TRAF5, Sci. Signal. 5 (2012) ra81.

30. H. Ishikawa, G.N. Barber, STING is an endoplasmic reticulum adaptor that facilitates innate immune signalling, Nature 455 (2008) 674–678.

31. Y. Tanaka, Z.J. Chen, STING specifies IRF3 phosphorylation by TBK1 in the cytosolic DNA signaling pathway, Sci. Signal. 5 (2012) ra20.

32. Z.T. Varga, A. Grant, B. Manicassamy, P. Palese, Influenza virus protein PB1-F2 inhibits the induction of type I interferon by binding to MAVS and decreasing mitochondrial membrane potential, J. Virol. 86 (2012) 8359–8366.

33. Y. Yang, Y. Liang, L. Qu, Z. Chen, M. Yi, K. Li, S.M. Lemon, Disruption of innate immunity due to mitochondrial targeting of a picornaviral protease precursor, Proc.Natl. Acad. Sci. U. S. A. 104 (2007) 7253–7258.

34. T. Muta, D. Kang, S. Kitajima, T. Fujiwara, N. Hamasaki, p32 protein, a splicing factor 2-associated protein, is localized in mitochondrial matrix and is functionally important in maintaining oxidative phosphorylation, J. Biol. Chem. 272 (1997) 24363–24370.

35. L. Xu, N. Xiao, F. Liu, H. Ren, J. Gu, Inhibition of RIG-I and MDA5-dependent antiviral response by gC1qR at mitochondria, Proc. Natl. Acad. Sci. U. S. A. 106 (2009) 1530–1535.

FIGURE LEGENDS

Figure. 1. Structural and functional analyses of MAVS constructs using a BRET assay. (A). HEK293 cells were transfected with empty (mock) or increasing amounts (5, 20, and 50 ng) of expression vector for Venus-MAVS and with either IFN-β (left) or NF-κB (right) luciferase reporter plasmids. The far right lane (NS3/4A) of both panels indicates that 20 ng of HA-tagged NS3/4A expression plasmid was co-transfected in the cells (using 50 ng Venus-MAVS). (B). Western blots of post-nuclear lysates from the reporter assay (A) were developed by immunoblotting with the indicated antibodies. Anti-β-actin was used as a loading control of each sample. (C). HEK293 cells were co-transfected with 5 ng Rluc-MAVS expression plasmid with increasing amounts (0−200 ng) of Venus-tagged MAVS, Tom-22, or Omp-25 plasmids, and analyzed 20 h later using a BRET saturation assay. (D). HEK 293 cells were co-transfected with their pairs of Rluc-MAVS (WT)/Venus-MAVS (WT), Rluc-MAVS (201–540)/Venus-MAVS (201–540), or Rluc-MAVS (1–514)/Venus-MAVS (1–514), and a BRET saturation assay was performed. The plasmids used in the assay were Rluc vectors (5 ng) and increasing amounts (0−200 ng) of Venus plasmids, respectively. Graphs are plotted as a function of the ratio of the fluorescence of the acceptor (Venus) to the luminescence of the donor (Rluc). (E). HEK293 cells were co-transfected with 50 ng of empty (mock) or the indicated MAVS plasmids, and the luciferase reporter plasmid p125luc. Inset: 1, Venus-MAVS; 2, Venus-MAVS (1-514); 3, Venus-MAVS(201-540). Transfected cells were analyzed 24 h later for IFN-β-dependent luciferase activity.

The presence of MAVS variants was confirmed by Western blotting with a monoclonal antibody against GFP. All data shown represent mean values±s.d. (n=3). ***P<0.001.

Figure. 2. MAVS forms highly ordered oligomers. (A). HEK293 cells were transfected with either Venus-MAVS, Venus(N)-MAVS, Venus(C)-MAVS, or equal mass pairs of Venus(N)- and Venus(C)-MAVS expression plasmids, and the cells were visualized by fluorescence microscopy (left panels) or the fluorescence was quantified using a luminometer (right panel). (B). Bimolecular fluorescence complementation (BiFC) BRET saturation assay was performed using (A), except that the cells were co-transfected with 5 ng of the Rluc-MAVS construct. All data shown represent mean values±s.d. (n=3). (C). Electron micrographs of mitochondrial morphologies in wild-type MEF cells infected with (right) and without (left) SeV (MOI of 5) for 20 h. Note the inhomogeneous broadening of the mitochondrial intermembrane space (red arrowheads) in the infected MEFs (right panel). Scale bar, 500 nm.

Figure. 3. NS3/4A abolishes MAVS oligomerization. (A). Schematic representation of wild-type (WT) MAVS on the mitochondrial outer membrane (left panel). The HCV protease, NS3/4A, cleaves MAVS at the Cys-508 position. Asterisks indicate Cys-508 residue mutated (Arg) in this study. For

simplicity, conformation of the oligomerized MAVS is depicted as a few molecules. (B). HEK293 cells were transfected with empty (mock) or increasing amounts (5, 20, and 50 ng) of expression vector for mutant Venus-MAVS (C508R) and with either IFN-β (left) or NF-κB (right) luciferase reporter plasmids. The far right lane (NS3/4A) of each panel indicates that 20 ng of HA-tagged NS3/4A expression plasmid was co-transfected in the cells (using 50 ng of mutant MAVS construct). All data shown represent mean values±s.d. (n=3). **P<0.005 and ***P<0.001, respectively. (C). Western blots of post-nuclear lysates from the reporter assay (B) were developed by immunoblotting with the indicated antibodies. Anti-β-actin was used as the loading control for each sample. (D). HEK293 cells were co-transfected with 5 ng of Rluc-tagged MAVS constructs and increasing amounts (0−200 ng) of Venus-tagged MAVS plasmids along with (red and yellow) or without (blue and green) HA-tagged NS3/4A plasmid (100 ng). Graphs of BRET saturation assays are plotted as a function of the ratio of the fluorescence of the acceptor (Venus) to the luminescence of the donor (Rluc). Squares, WT construct; triangles, mutant construct.

Figure. 4. BRET saturation assays in the presence of NLRX1 and its variants. (A). HEK293 cells were co-transfected with 5 ng of the Rluc-MAVS expression plasmid and increasing amounts (0−200 ng) of the Venus-MAVS plasmid along with either 100 ng of NLRX1 or control (mock) plasmids, and

were analyzed 20 h later using a BRET saturation assay. In this assay, we used a matrix-targeted DHFR (mtDHFR) plasmid as the mock. (B). HEK293 cells were transfected with the NLRX1 expression plasmid, and the purified mitochondrial fraction from the cells was treated with trypsin (100 μg/mL) in the absence (−) or presence (+) of 0.05% digitonin. The reactants were determined by Western blot analysis with several mitochondrial protein antibodies as indicated. Mitochondrial outer membrane proteins: MAVS, Mfn1, Mfn2, and Tom20. Intermembrane space protein: cytochrome c. Inner membrane proteins: OPA-1 and Cox IV. Matrix protein: mtHsp70. (C). Similar to (A), except that 100 ng of NLRX1 variant plasmids was used. All data shown represent mean values±s.d. (n=3). ***P<0.01. (D). Subcellular localization of NLRX1 variants was monitored by confocal microscopy. The indicated constructs (HA-tagged) were retrovirally expressed in NLRX1-deficient MEFs and immunofluorescence against the HA epitope (green), and mitochondria were labeled with a mitochondrial-targeted red fluorescent protein. Each image is a single confocal section from selected cells (scale bar, 10 μm), and enlarged views of the boxed area are shown in the inset column (scale bar, 5 μm).

Figure. 5. MAVS oligomerization is blocked by Mfn2 and it variants. (A). HEK293 cells were co-transfected with 5 ng of the Rluc-MAVS expression plasmid with increasing amounts (0−200 ng) of

the Venus-MAVS plasmid along with 100 ng of each Myc-tagged Mfn1, Mfn2, or control (mock) plasmids, and analyzed 20 h later using a BRET saturation assay. (B). Similar to (A), except that 100 ng of Mfn2 variant plasmids was used. Right panels show Western blots of post-nuclear lysates from the BRET saturation point of each curve by immunoblotting with the indicated antibodies. (C). HEK293 cells were co-transfected with an equal mass of Venus(N)-MAVS and Venus(C)-MAVS expression plasmids together with the indicated expression plasmids, and the fluorescence signals were quantified using a luminometer. (D). BiFC BRET experiment using (C), except that the cells were co-transfected with 5 ng of the Rluc-MAVS construct. In these BRET assays, we used an Omp-25 expression plasmid as the control (mock) for the integral outer mitochondrial membrane protein. All data shown represent mean values±s.d. (n=3). ***P<0.01.

Figure. 6. A schematic model of MAVS activation and its inhibition by negative regulators. (A). Viral infection can activate RLRs, leading to their translocation to their adaptor protein, MAVS, on the mitochondrial surface. These associations trigger changes in the MAVS concentration on the mitochondrial membrane foci (top). We propose that the driving forces of their interactions come from both the MAVS conformational changes and the membrane dynamics (red arrows). The MAVS homogeneous oligomers (top) recruit various signaling molecules that are involved in MAVS

signaling. To simplify the figure, the upstream event of the RLRs–MAVS interaction via a CARD–CARD domain is not illustrated. (B). Three different types of MAVS inhibition are illustrated. X in the middle panel indicates a mitochondrial factor that links MAVS with NLRX1 and might act to negatively regulate MAVS signaling. OM, mitochondrial outer membrane; IM, mitochondrial inner membrane; $\Delta\Psi_m$, mitochondrial membrane potential.

Supplementary Fig. S1. Functional analysis of the Rluc-MAVS construct. HEK293 cells were transfected with empty (mock) or increasing amounts (5, 20, and 50 ng) of expression vector for Rluc-MAVS. The far right lane (NS3/4A) indicates that 20 ng of HA-tagged NS3/4A expression plasmid was co-transfected in the cells (using 50 ng Rluc-MAVS). Western blots of post-nuclear lysates were developed by immunoblotting with the indicated antibodies. Anti-β-actin was used as a loading control for each sample.

Supplementary Fig. S2. BRET saturation assay between Rluc and Venus. HEK293 cells were co-transfected with their pairs of Rluc-MAVS/Venus-MAVS (filled squares), Rluc/Venus-MAVS (open squares), or Rluc/Venus (open circles), and a BRET saturation assay was performed. The plasmids

used in the assay were Rluc vectors (5 ng) and increasing amounts (0-200 ng) of Venus plasmids, respectively. All data shown represent mean values ± s.d. (n=3).

Supplementary Fig. S3. Structure of Venus-MAVS variants used in the present study. Venus protein (27 kDa) is fused at the N-terminus of each MAVS construct.

Supplementary Fig. S4. MAVS variants lacking their functional domains show impaired activation of both NF-kB and ISRE. HEK293 cells were co-transfected with 50 ng of empty (mock) or indicated MAVS plasmids and either the luciferase reporter plasmid pELAM or pISRE-Luc. At 24 hr, transfected cells were analyzed for NF-kB- and ISRE-dependent luciferase activities. All data shown represent mean values ± s.d. (n=3). ***P < 0.001.

Supplementary Fig.S5. Schematic diagram of (A) BRET and (B) BiFC BRET systems used in the study. C and N in (B) represent the N-terminal truncated version of Venus and its C-terminal truncated proteins fused with MAVS, respectively.

Supplementary Fig.S6. Electron micrographs of mitochondrial morphologies in MEFs infected with and without SeV. Left panels (uninfected cells) and right panels (infected cells). Scale bar, 500 nm.

Supplementary Fig.S7. Mitochondrial fractionation study of the C-terminal HA-tagged version of the NLRx1 construct. HEK293 cells were transfected with the NLRX1-C-terminal HA-tagged expression plasmid, and the purified mitochondrial fraction from the cells was treated with trypsin (100 μg/mL) in the absence (-) or presence (+) of 0.05% (w/v) digitonin. The reactants were determined by Western blot analysis with the indicated mitochondrial protein antibodies. Mitochondrial outer membrane proteins: MAVS, Mfn1, and Mfn2, Inner membrane proteins: OPA-1 and Cox IV. Matrix protein: Hsp60.

Supplementary Fig.S8. BRET saturation assays in the presence of Tfam and its variant lacking the mitochondrial targeting sequence. HEK293 cells were co-transfected with 5 ng of the Rluc-MAVS expression plasmid and increasing amounts (0-200 ng) of the Venus-MAVS plasmid along with 10 ng each of Tfam, its variant (lacking MTS), or control (mock) plasmids, and analyzed 20 hr

later using a BRET saturation assay. In this assay, we used a matrix-targeted DHFR (mtDHFR) plasmid as the mock. All data shown represent mean values ± s.d. (n=3).

Supplementary Fig.S9. Mfn2 affects MAVS-MAVS interactions in a dose-dependent manner. HEK293 cells were co-transfected with 5 ng of the Rluc-MAVS expression plasmid with increasing amounts (0-200 ng) of the Venus-MAVS plasmid along with 50 (open triangles), or 100 ng (open squares) of Myc-tagged Mfn2, or 100 ng of control (filled squares) plasmids, and analyzed 20 hr later with a BRET saturation assay. In this BRET assay, we used an Omp-25 expression plasmid as the control for the integral outer mitochondrial membrane protein. All data shown represent mean values ± s.d. (n=3). ***P < 0.01.

Supplementary Fig.S10. Schematic diagram of full-length human Mfn2 and its variants used in the study. All Mfn2 constructs have a Myc-tag attached at the C-terminus.

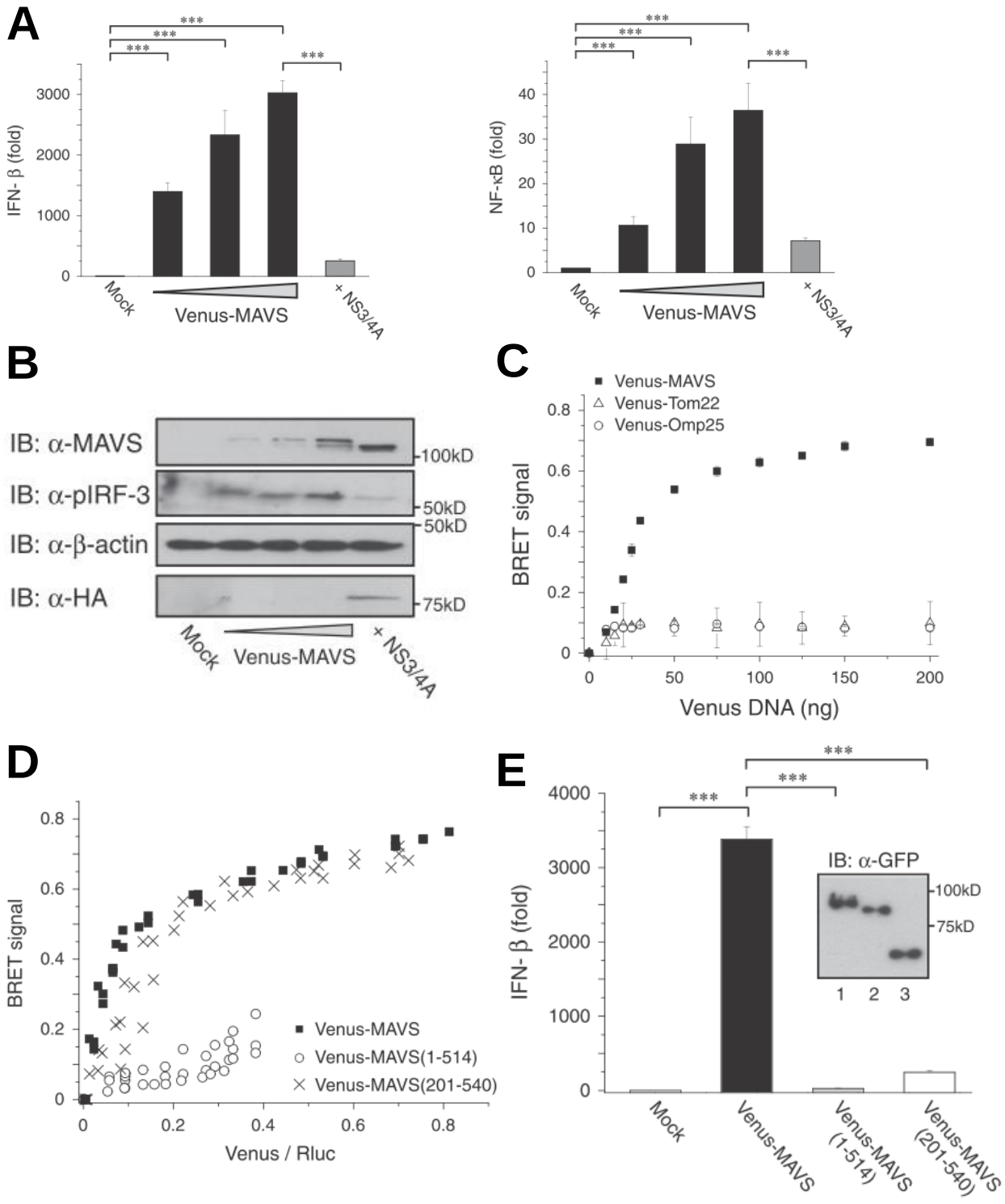
A
IFN- β (fold)
NF-κB (fold)
Mock
Venus-MAVS
+ NS3/4A
***
B
IB: α-MAVS
IB: α-pIRF-3
IB: α-β-actin
IB: α-HA
100kD
50kD
50kD
75kD
C
Venus-MAVS
Venus-Tom22
Venus-Omp25
BRET signal
Venus DNA (ng)
D
BRET signal
Venus / Rluc
Venus-MAVS
Venus-MAVS(1-514)
Venus-MAVS(201-540)
E
IFN- β (fold)
IB: α-GFP
100kD
75kD
1 2 3
Mock
Venus-MAVS
Venus-MAVS (1-514)
Venus-MAVS (201-540)

Figure 1

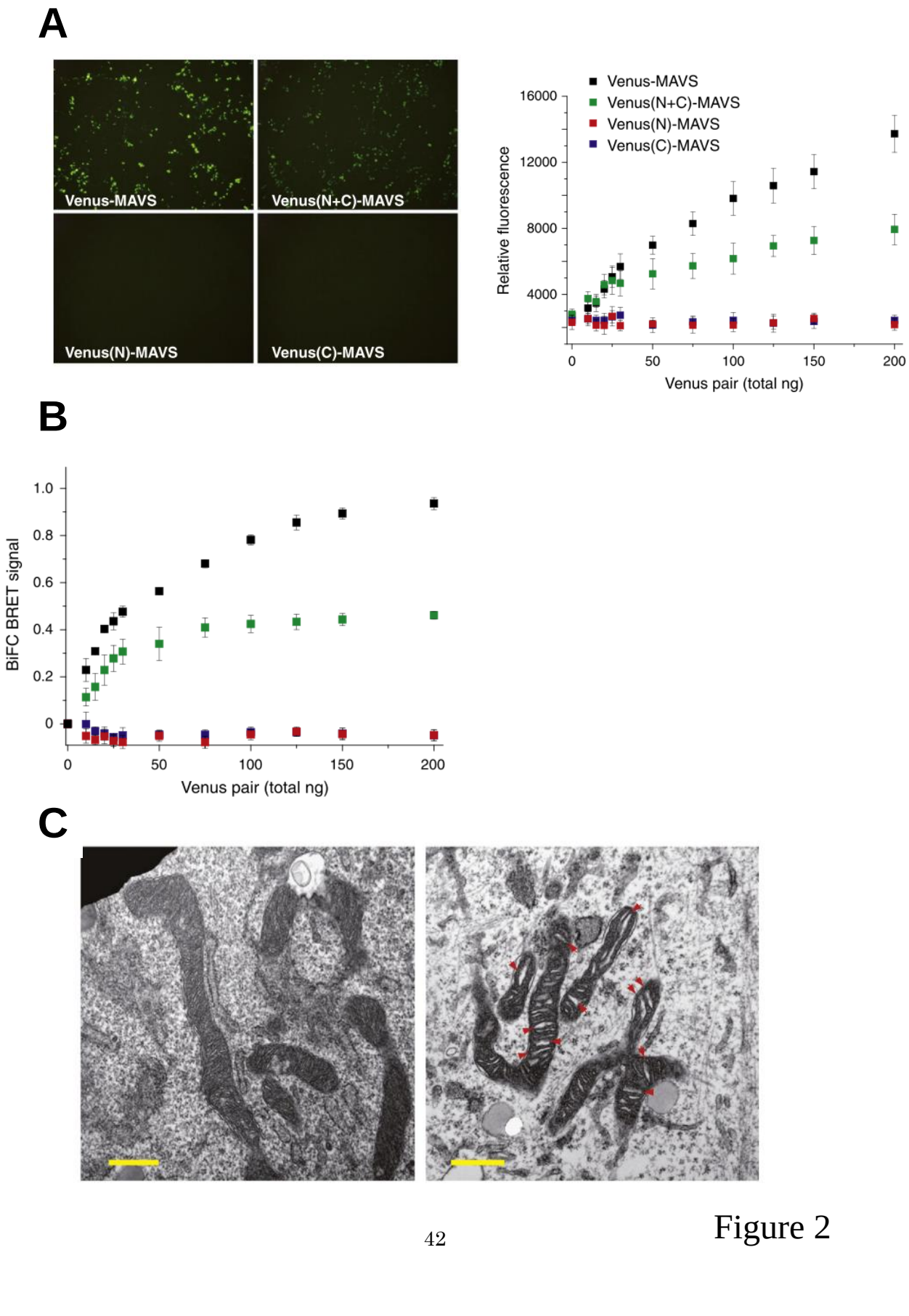
A
Venus-MAVS
Venus(N+C)-MAVS
Venus(N)-MAVS
Venus(C)-MAVS
Venus-MAVS
Venus(N+C)-MAVS
Venus(N)-MAVS
Venus(C)-MAVS
Relative fluorescence
16000
12000
8000
4000
0
50
100
150
200
Venus pair (total ng)
B
BiFC BRET signal
1.0
0.8
0.6
0.4
0.2
0
0
50
100
150
200
Venus pair (total ng)
C

Figure 2

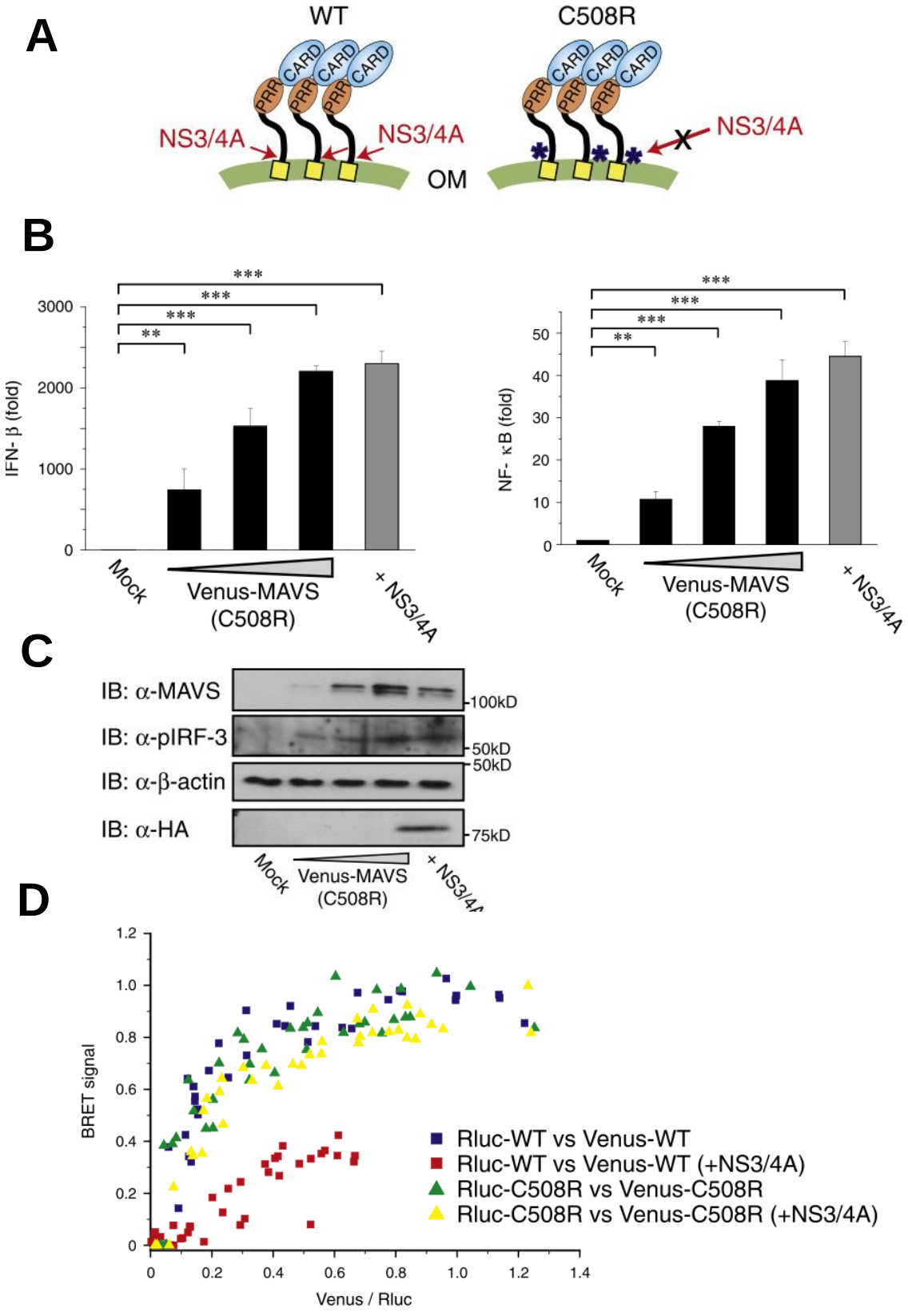
A
WT
C508R
CARD
PRR
NS3/4A
OM
X
B
IFN- β (fold)
NF- κB (fold)
Mock
Venus-MAVS
(C508R)
+NS3/4A
C
IB: α-MAVS
IB: α-pIRF-3
IB: α-β-actin
IB: α-HA
100kD
50kD
75kD
D
BRET signal
Venus / Rluc
Rluc-WT vs Venus-WT
Rluc-WT vs Venus-WT (+NS3/4A)
Rluc-C508R vs Venus-C508R
Rluc-C508R vs Venus-C508R (+NS3/4A)

Figure 3

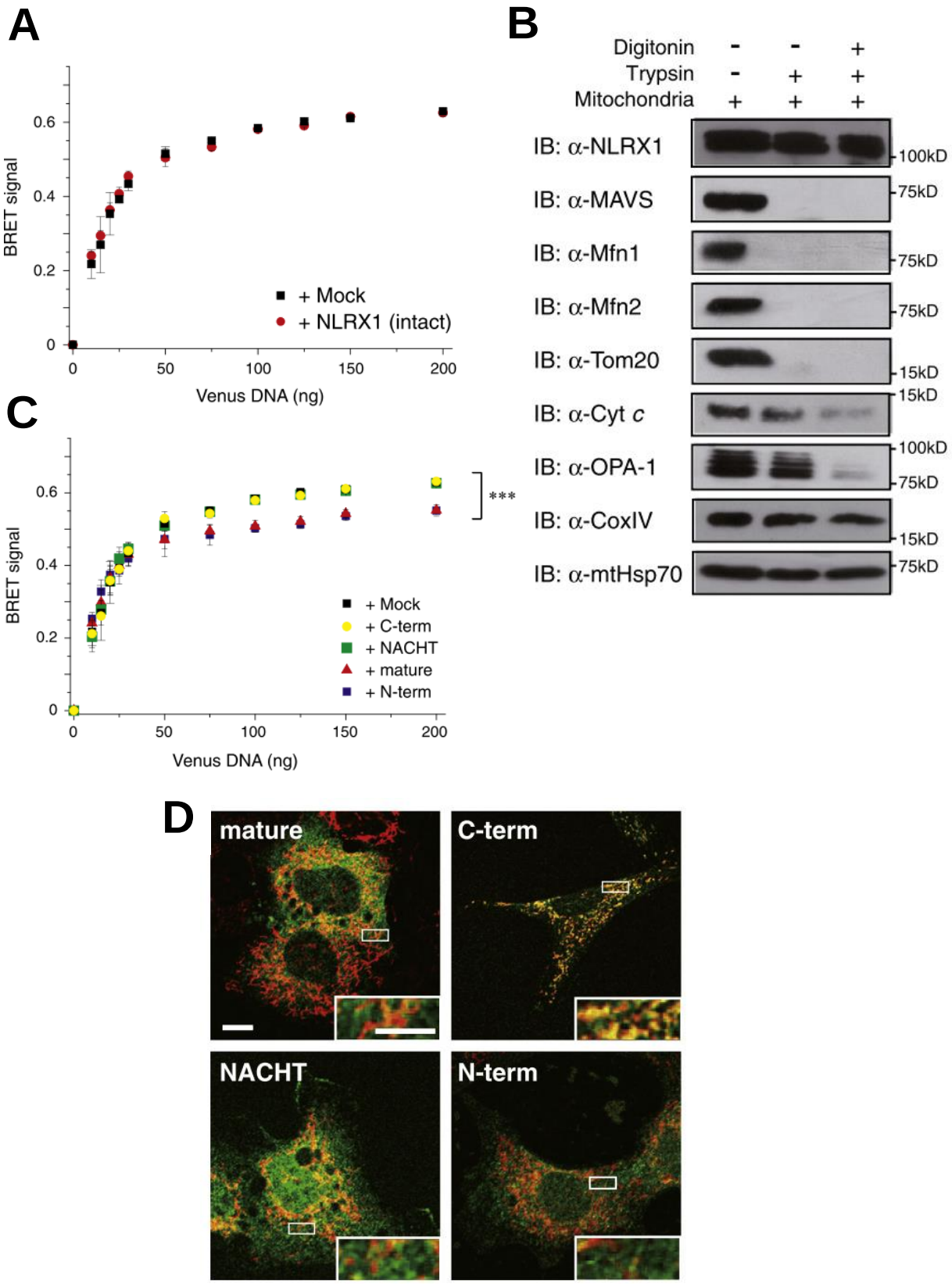
A
BRET signal
0
0.2
0.4
0.6
0
50
100
150
200
Venus DNA (ng)
+ Mock
+ NLRX1 (intact)
B
Digitonin - - +
Trypsin - + +
Mitochondria + + +
IB: α-NLRX1
IB: α-MAVS
IB: α-Mfn1
IB: α-Mfn2
IB: α-Tom20
IB: α-Cyt c
IB: α-OPA-1
IB: α-CoxIV
IB: α-mtHsp70
100kD
75kD
75kD
75kD
15kD
15kD
100kD
75kD
15kD
75kD
C
BRET signal
0
0.2
0.4
0.6
0
50
100
150
200
Venus DNA (ng)
***
+ Mock
+ C-term
+ NACHT
+ mature
+ N-term
D
mature
C-term
NACHT
N-term

Figure 4

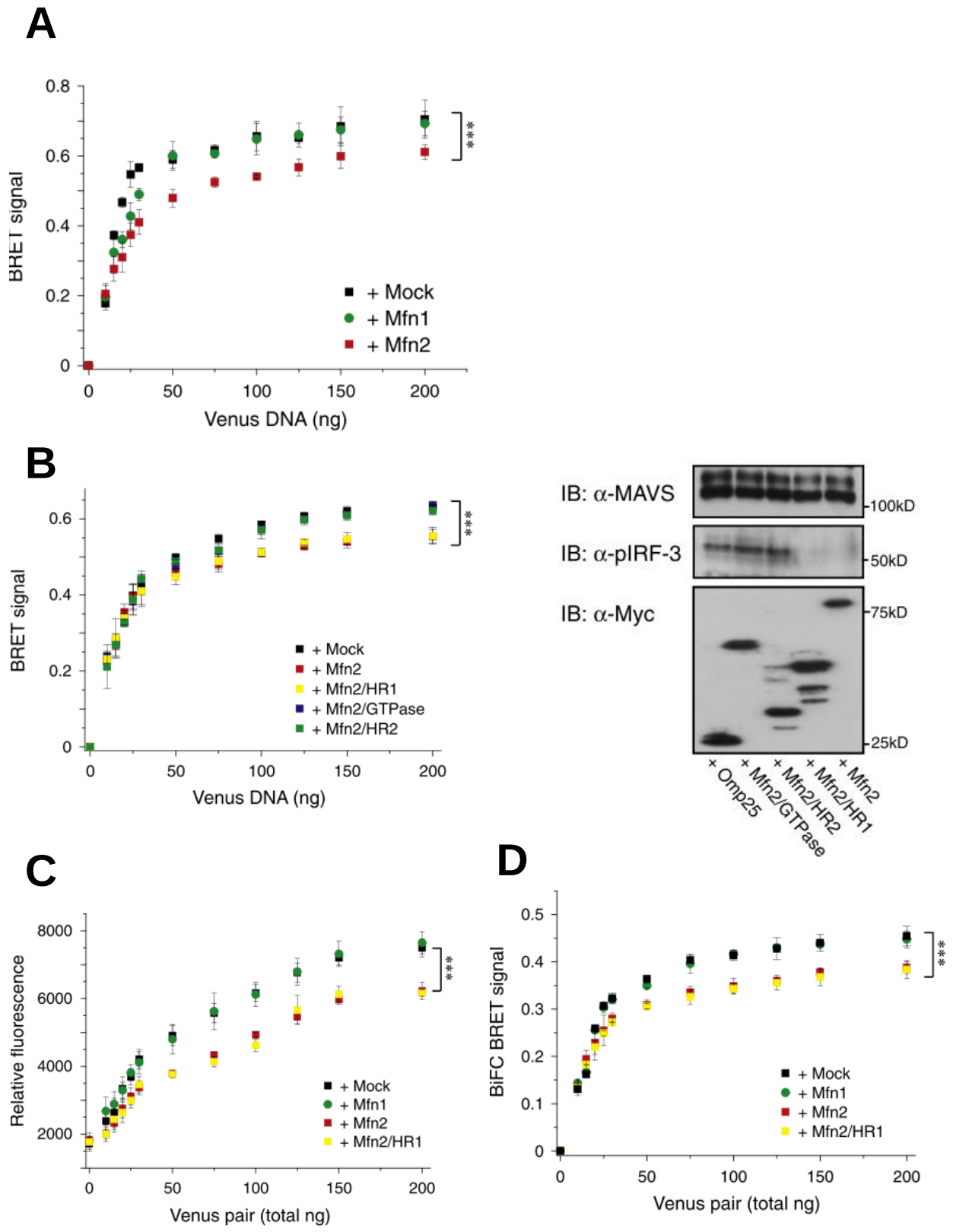
A
BRET signal
Venus DNA (ng)
+ Mock
+ Mfn1
+ Mfn2
***
B
BRET signal
Venus DNA (ng)
+ Mock
+ Mfn2
+ Mfn2/HR1
+ Mfn2/GTPase
+ Mfn2/HR2
***
IB: α-MAVS
IB: α-pIRF-3
IB: α-Myc
100kD
50kD
75kD
25kD
× Omp25
× Mfn2/GTPase
× Mfn2/HR2
× Mfn2/HR1
× Mfn2
C
Relative fluorescence
Venus pair (total ng)
+ Mock
+ Mfn1
+ Mfn2
+ Mfn2/HR1
***
D
BiFC BRET signal
Venus pair (total ng)
+ Mock
+ Mfn1
+ Mfn2
+ Mfn2/HR1
***

Figure 5

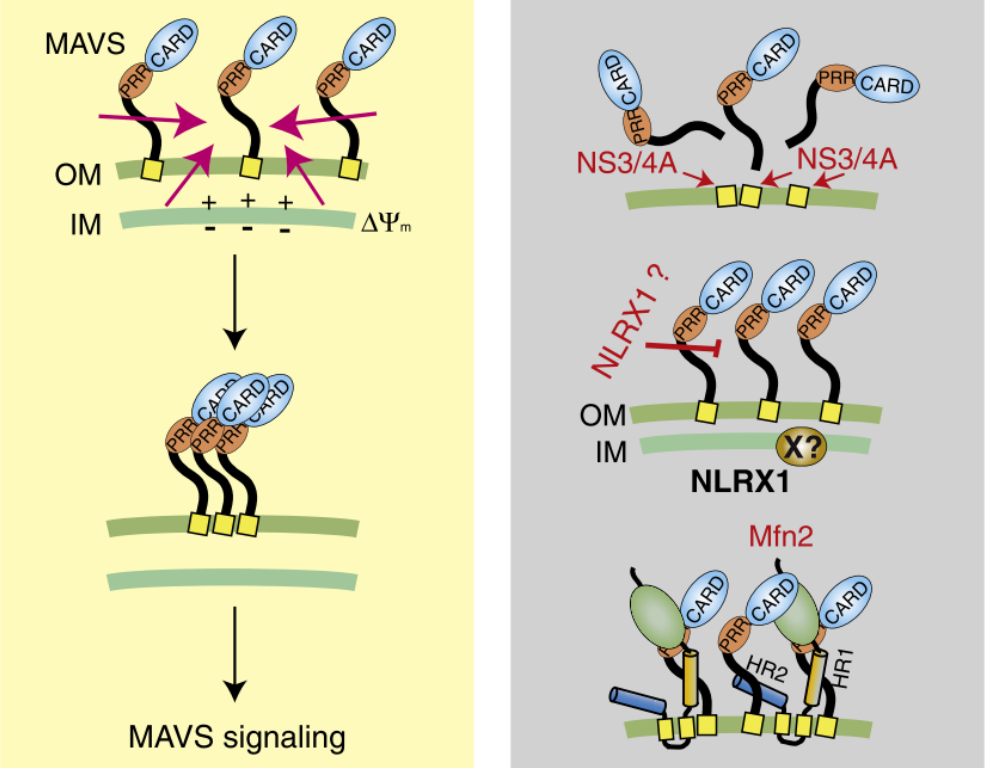
MAVS
PRR
CARD
OM
IM
+ + +
- - -
ΔΨm
MAVS signaling
NS3/4A
NS3/4A
NLRX1 ?
OM
IM
X?
NLRX1
Mfn2
HR2
HR1

Figure 6

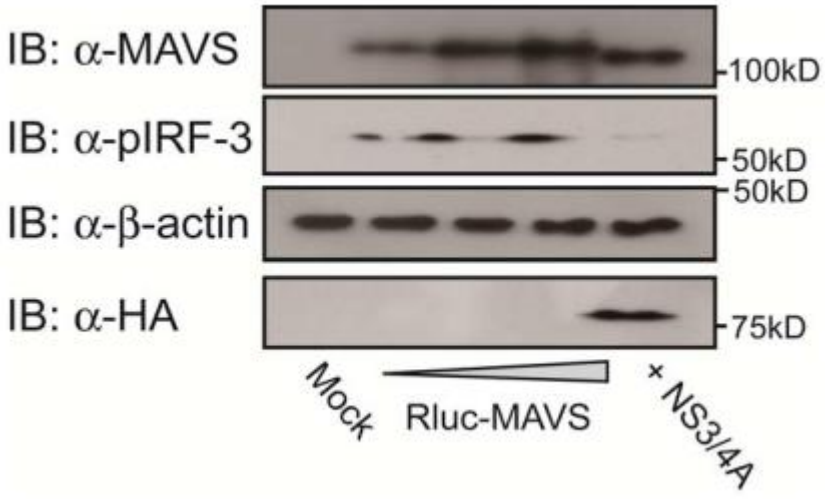
IB: α-MAVS
IB: α-pIRF-3
IB: α-β-actin
IB: α-HA
100kD
50kD
50kD
75kD
Mock
Rluc-MAVS
+ NS3/4A

Figure S1

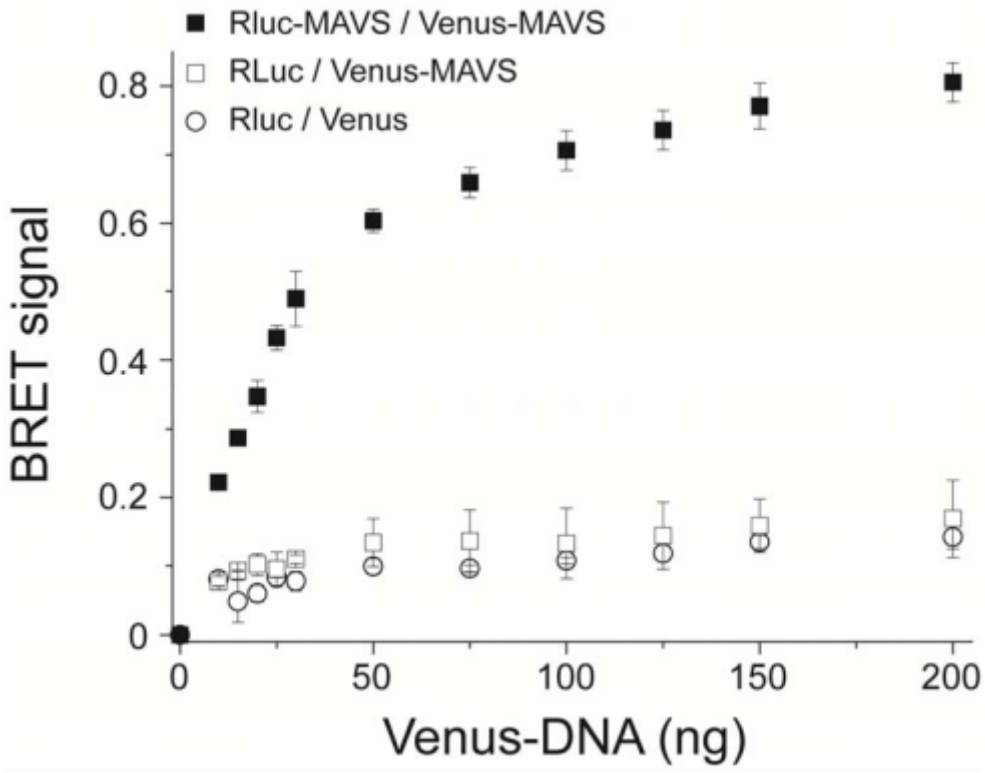
Rluc-MAVS / Venus-MAVS
RLuc / Venus-MAVS
Rluc / Venus
BRET signal
0
0.2
0.4
0.6
0.8
0
50
100
150
200
Venus-DNA (ng)

Figure S2

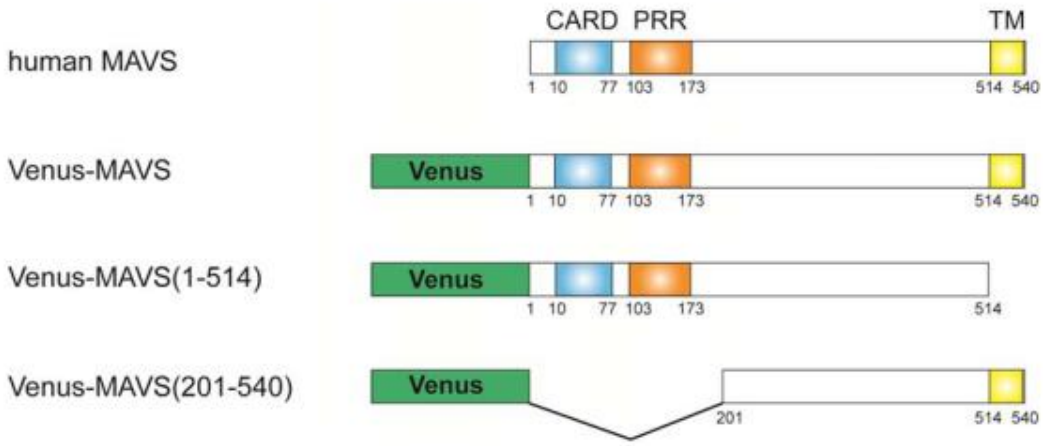
CARD
PRR
TM
human MAVS
1 10 77 103 173
514 540
Venus-MAVS
Venus
1 10 77 103 173
514 540
Venus-MAVS(1-514)
Venus
1 10 77 103 173
514
Venus-MAVS(201-540)
Venus
201
514 540

Figure S3

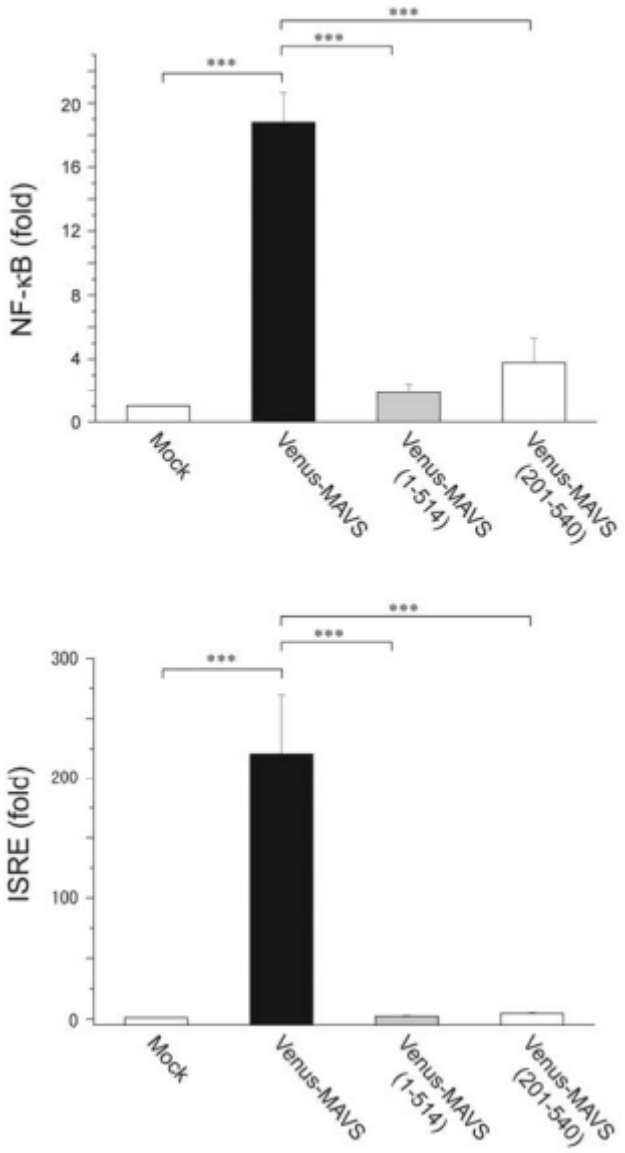
***
***
***
NF-κB (fold)
20
16
12
8
4
0
Mock
Venus-MAVS
Venus-MAVS (1-514)
Venus-MAVS (201-540)
***
***
***
ISRE (fold)
300
200
100
0
Mock
Venus-MAVS
Venus-MAVS (1-514)
Venus-MAVS (201-540)

Figure S4

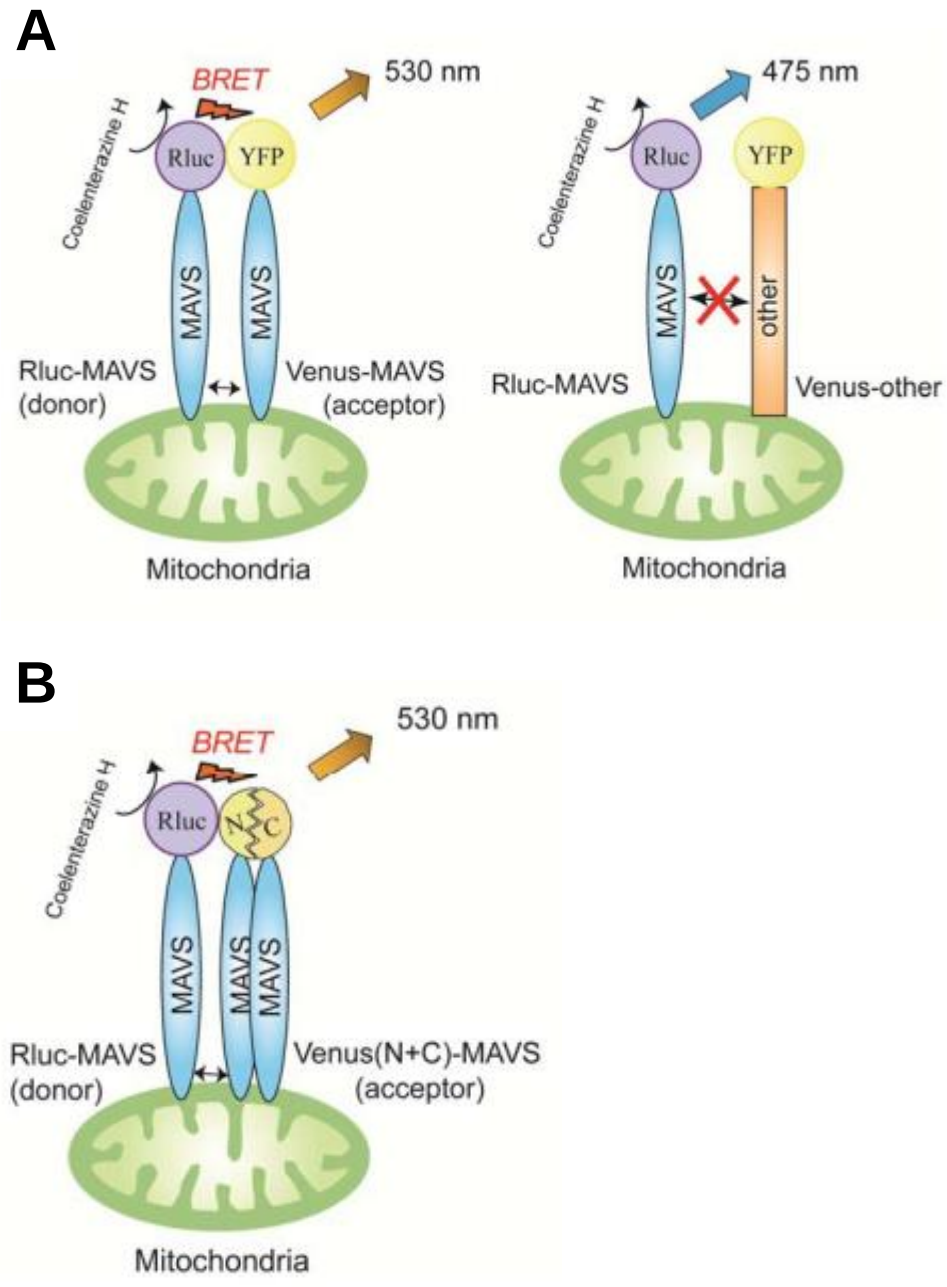
A
BRET
530 nm
Coelenterazine H
Rluc
YFP
MAVS
MAVS
Rluc-MAVS
(donor)
Venus-MAVS
(acceptor)
Mitochondria
475 nm
Coelenterazine H
Rluc
YFP
MAVS
other
Rluc-MAVS
Venus-other
Mitochondria
B
BRET
530 nm
Coelenterazine H
Rluc
N
C
MAVS
MAVS
MAVS
Rluc-MAVS
(donor)
Venus(N+C)-MAVS
(acceptor)
Mitochondria

Figure S5

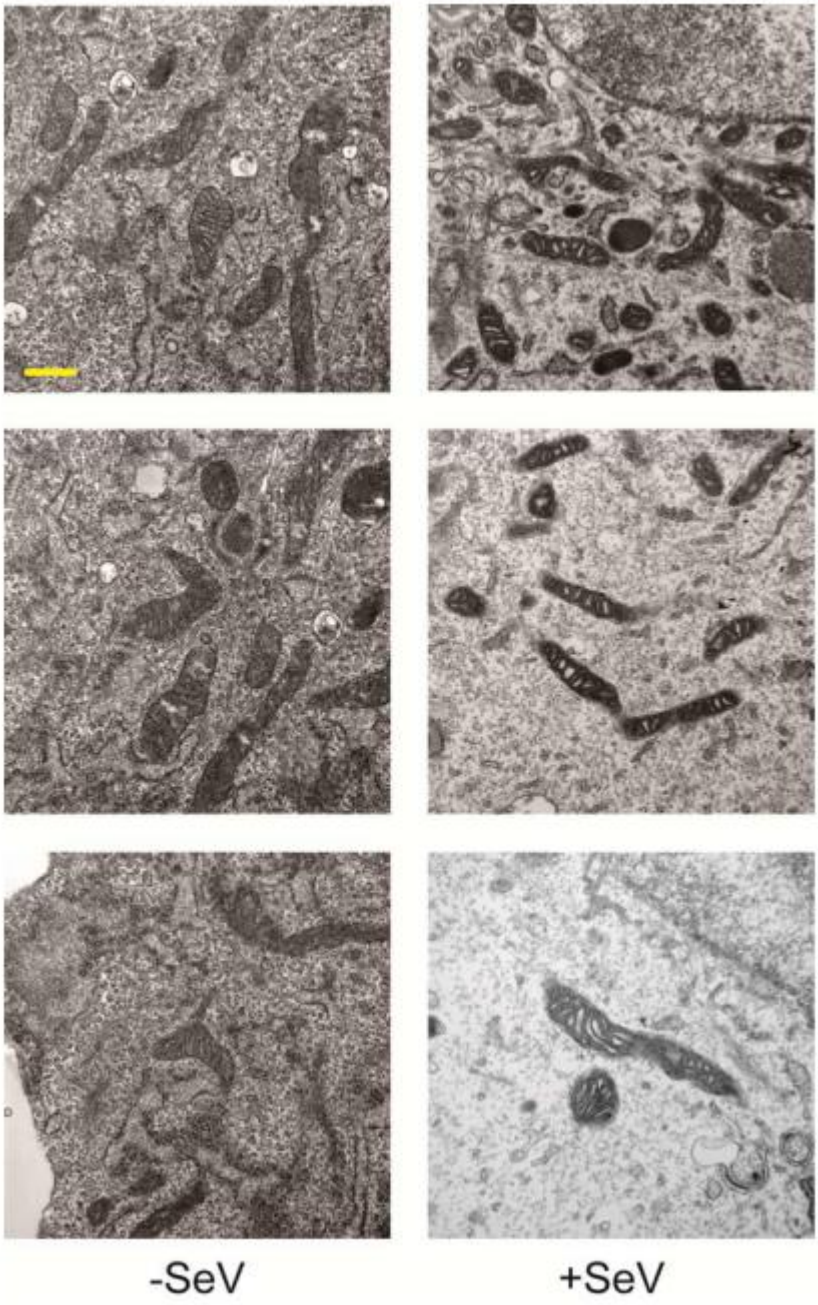

Figure S6

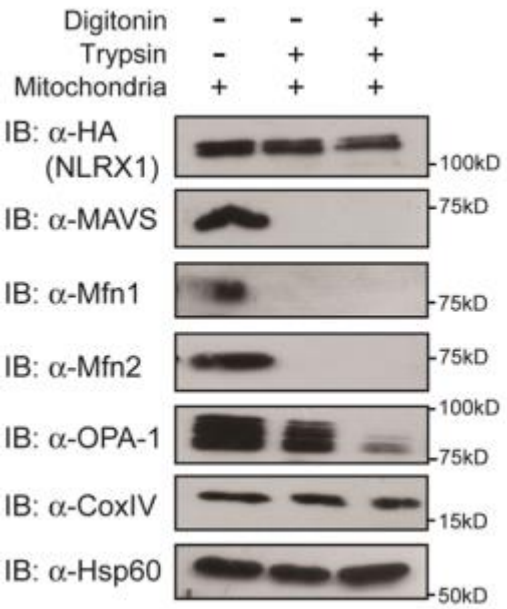
Digitonin - - +
Trypsin - + +
Mitochondria + + +
IB: α-HA (NLRX1)
100kD
IB: α-MAVS
75kD
IB: α-Mfn1
75kD
IB: α-Mfn2
75kD
IB: α-OPA-1
100kD
75kD
IB: α-CoxIV
15kD
IB: α-Hsp60
50kD

Figure S7

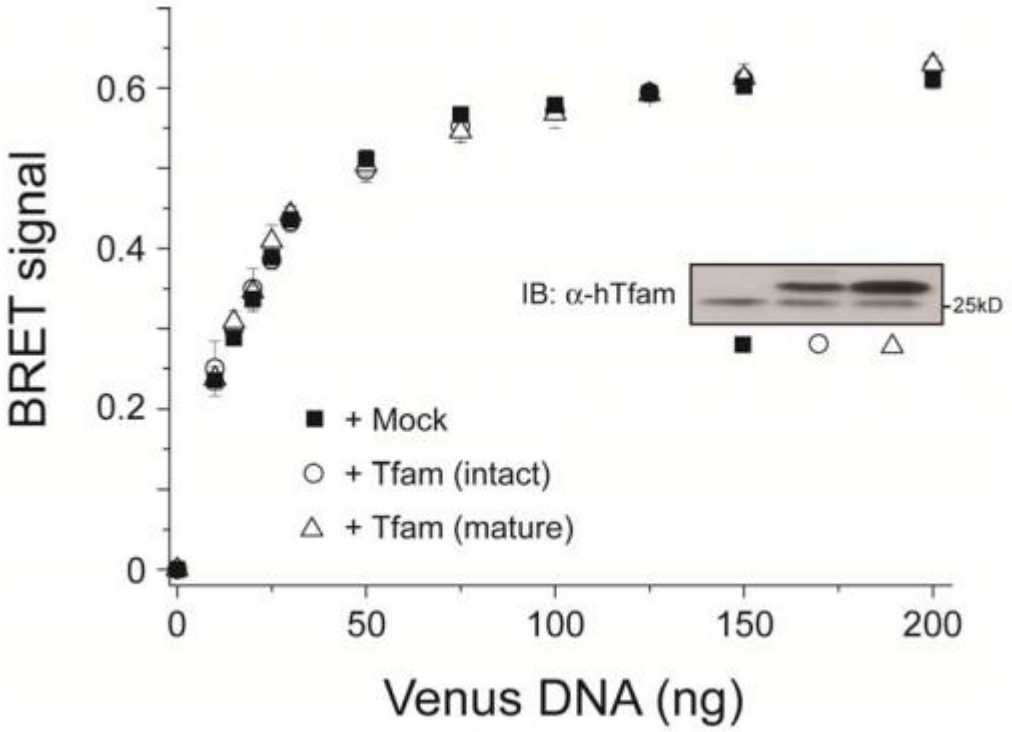
BRET signal
0.6
0.4
0.2
0
0
50
100
150
200
Venus DNA (ng)
IB: α-hTfam
25kD
+ Mock
+ Tfam (intact)
+ Tfam (mature)

Figure S8

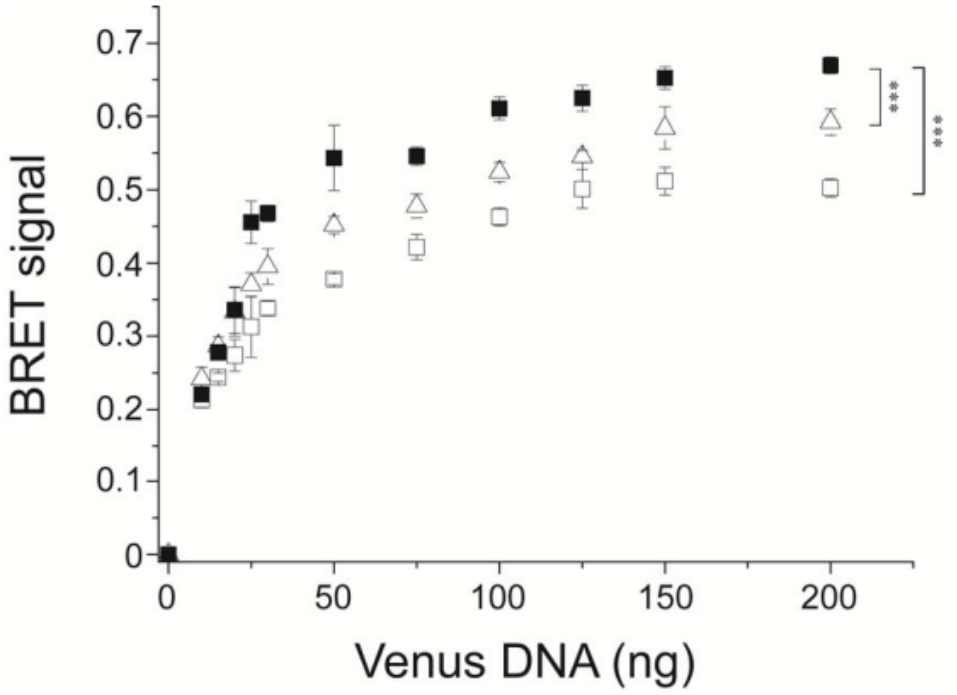

Figure S9

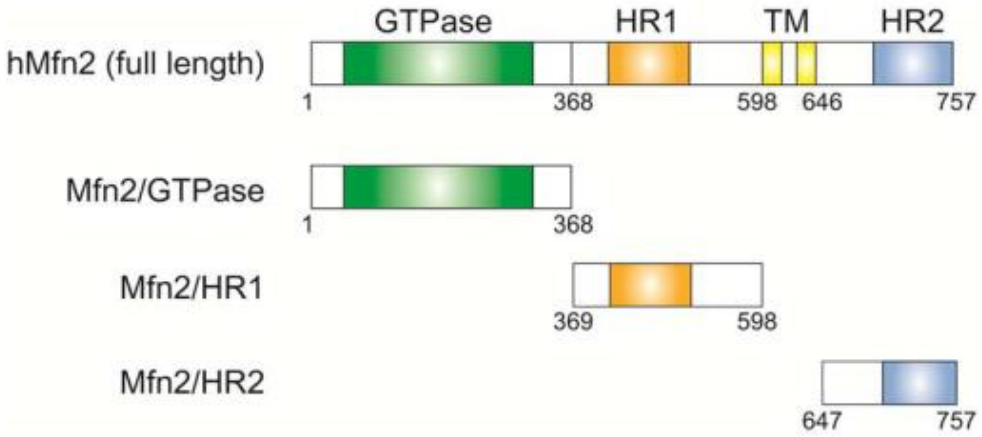
GTPase
HR1
TM
HR2
hMfn2 (full length)
1
368
598
646
757
Mfn2/GTPase
1
368
Mfn2/HR1
369
598
Mfn2/HR2
647
757

Figure S10

PART2

Analysis of the homotypic interaction of caspase-4/11 on cytoplasmic lipopolysaccharide by bioluminescence resonance energy transfer

ABBREVIATIONS

NLRs; Nod-like receptors

CARD; caspase-recruitment domain

BRET; bioluminescence resonance energy transfer

rCasp4/11; recombinants of caspase-4/11

GnTI; *N*-acetylglucosaminyltransferase I

*Ec*LPS; LPS prepared from *Escherichia coli*

*Rs*LPS; LPS prepared from *Rhodobacter sphaeroides*

Rluc; *Renilla* luciferase

MDP; muramyl dipeptide

BiFC; bimolecular fluorescent complementation

SUMMARY

Mouse caspase-11 and its human homologue caspase-4 are activated by direct binding with cytoplasmic LPS through the N-terminal caspase-recruitment domain to induce pyroptosis, independently of Toll-like receptor 4, and canonical inflammasomes, suggesting that binding of LPS to caspase-4/11 induces self-oligomerization and autocatalytic activation. Here we examined homotypic protein-protein interactions between caspase-4/11 (rCasp4/11) recombinants expressed in an HEK293 cell line using bioluminescence resonance energy transfer (BRET). BRET combined with functional analysis revealed specific protein-protein interactions between rCasp4/11 molecules with the fused BRET tags approaching within 10 nm, which was dependent on LPS from *Escherichia coli* O111:B4 (*Ec*LPS*)* that was incorporated by electroporation. Bimolecular fluorescence complementation of BRET tags combined with the BRET system showed no significant BRET signal between rCasp4 molecules, suggesting that rCasp4 forms a dimer but not higher molecular-weight oligomers on *Ec*LPS, or that rCasp4 forms at least a trimer, but the protein-protein interactions of rCasp4 molecules in the complex cause the BRET tags to be inappropriately oriented, thereby preventing BRET. Moreover, an antagonist LPS from *Rhodobacter sphaeroides* (*Rs*LPS) reduced the BRET efficiency between rCasp4/11 molecules by half compared to that of the *Ec*LPS. These findings indicate that the protein interactions by oligomers of rCasp4/11 on *Rs*LPS are not sufficient to induce

a highly efficient BRET signal, and that homotypic complex formation of caspase-4/11 on *Rs*LPS does not induce autocatalytic activation to trigger pyroptosis.

INTRODUCTION

Intracellular proinflammatory caspases, cysteine proteases, including caspase-1, -4, -5, and -11, play essential roles in innate immunity (1). Caspase-1 is activated on the specific signaling platforms known as inflammasomes that contain cytoplasmic Nod-like receptors (NLRs)[3], such as NLRP3, NLRP1, and NLRC4, which trigger a form of programmed necrosis known as pyroptosis and secretion of IL-1β/18 (2). The NLRs recognize not only microbe-associates molecular patterns, but also host-derived danger-associated molecular patterns secreted by activated immune cells or passively released by damaged cells (3). In addition to the canonical inflammasomes containing caspase-1, a non-canonical inflammasome was in mouse macrophages, showing that mouse caspase-11 is activated by intracellular LPS of Gram-negative bacteria, independently of the LPS receptor, Toll-like receptor 4, to induce pyroptosis (4-6).

Recently, Shi *et al.* reported that mouse caspase-11 and its human homologue caspase-4 are activated by direct binding with LPS or the functional part of LPS, lipid A, through the N-terminal caspase-recruitment domain (CARD) of caspase-4/11 without the intermediation of the canonical inflammasomes (7). The authors developed an assay system for caspase-4/11-dependent pyroptosis, indicating that electroporation of LPS causes massive cell death of pyroptosis in Hela, HaCaT, HT29, or HL60 cells, which endogenously express caspase-4, but not caspase-4/11-negative cells such as HEK293T cells, although ectopic expression of wild-type caspase-4 in HEK293T cells renders

sufficient sensitivity to LPS electroporation (7). Moreover, they found that LPS induces oligomerization of recombinant proteins of caspase-4/11 with the catalytic cysteine mutant background by pore-limit native gel analysis and gel filtration chromatography, suggesting that caspase-4/11 directly recognizes cytoplasmic LPS to induce self-oligomerization and autocatalytic activation on LPS (7).

On the other hand, factor C of the horseshoe crab *Tachypleus tridentatus*, an LPS-sensitive serine protease zymogen involved in hemolymph coagulation, complement activation, and LPS-induced hemocyte exocytosis, is autocatalytically activated on the surface of LPS (8-11). Structure-function analyses of factor C revealed that the LPS binding site is present in the N-terminal Cys-rich region of the molecule and that it contains a tripeptide sequence comprising an aromatic residue flanked by two basic residues (-Arg^{36}-Trp^{37}-Arg^{38}-), which is important for LPS recognition (12). The innate immune response to LPS in horseshoe crabs is distinct from that in mammals, because it appears to rely on structural features that are conserved among LPS-recognizing proteins from diverse species. Moreover, we reported that the N-terminal Arg residue and the distance between the N-terminus and the tripartite of the LPS-binding site of factor C are essential elements for autocatalytic activation (13). We proposed that the N-terminal Arg of factor C is essential for inducing specific protein-protein interactions between the factor C molecules in close proximity and with proper orientation on the surface of LPS, leading to the self-oligomerization and autocatalytic activation (13). To clarify the

molecular mechanism of the autocatalytic activation of caspase-4/11 on LPS, we prepared several recombinants of caspase-4 or caspase-11 (rCasp4/11) expressed in a HEK293 mutant cell line and examined the protein-protein interactions between rCasp4/11 using bioluminescence resonance energy transfer (BRET) in living cells.

RESULTS

Validation of BRET Constructs of Recombinant Proteins of Caspase-11 – To confirm whether LPS-induced caspase-11 activation triggers pyroptosis, a recombinant protein of the full length of rCasp11 was stably expressed in an HEK293 mutant cell line lacking *N*-acetylglucosaminyltransferase I (HEK293S GnTI$^-$) with no endogenous expression of caspase-4/11. LPS prepared from *Escherichia coli* O111:B4 (*Ec*LPS) was incorporated into the cells by an efficient LPS transfection protocol using a commercial electroporation device, as previously reported (7). Living and dead cells were stained with fluorescent reagents, 3',6'-Di(*O*-acetyl)-4',5'-bis[*N*,*N*-bis(carboxymethyl)aminomethyl] fluorescein, tetraacetoxymethyl ester (Calcein-AM), and DAPI, respectively. Electroporation of *Ec*LPS caused massive cell death to produce DAPI-positive cells in a rCasp11-dependent manner (Fig. 1A). The DAPI-positive cells were increased in the LPS-incorporated cells, but not in the control cells without electroporation, indicating that rCasp11 detects cytoplasmic LPS to induce autocatalytic activation of rCasp11, causing pyroptosis in the cells (Fig. 1B).

BRET does not require external excitation by ultraviolet sources, and non-radioactive energy transfer from a donor enzyme of *Renilla* luciferase (Rluc) to a complementary acceptor fluorophore of a yellow fluorescence protein derivative (Venus) occurs after oxidation of an Rluc substrate coelenterazine H; the efficiency of the energy transfer is inversely proportional to the sixth power of

the distance between the donor and acceptor, and therefore, a comparable distance of biologic protein-protein interactions within 10 nm can be monitored in real time in living cells (14). We first designed two constructs, rCasp11-Rluc and rCasp11-Venus, containing either the Rluc- or Venus-fusion tag at the C-terminal portion of rCasp11. To examine whether the two fusion proteins detect cytoplasmic LPS to cause LPS-dependent pyroptosis, rCasp11-Rluc and rCasp11-Venus were simultaneously expressed in HEK293S GnTI$^-$ cells. Electroporation of *Ec*LPS into the cells induced massive cell death of the cells stably co-expressing rCasp11-Rluc and rCasp11-Venus, suggesting that addition of either of the tags to the C-terminal region of rCasp11 did not inhibit the LPS-dependent oligomerization and autocatalytic activation of rCasp11 (Figs. 1A and 1B).

Detection of Complex Formation of Caspase-11 on Cytoplasmic LPS by BRET assays – We next designed constructs of two recombinant proteins of caspase-11 with an active-site replacement of Cys^{254} to Ala^{254}, rCasp11(C/A)-Rluc and rCasp11(C/A)-Venus, to prevent the proteolytic activity of caspase-11. To elucidate the protein-protein interactions induced by cytoplasmic LPS between rCasp11(C/A)-Rluc and rCasp11(C/A)-Venus, we transfected *Ec*LPS into HEK293S GnTI$^-$ cells stably co-expressing the two fusion proteins with increasing concentrations by electroporation and monitored the resulting BRET signals. The BRET saturation assay displayed a hyperbolic curve with a plateau at ~0.01 μg/ml *Ec*LPS, characteristic of a specific protein-protein interaction, which was totally dependent on the amount of *Ec*LPS incorporated by electroporation (closed circles in Fig. 2).

The lipophilic part of LPS, lipid A, is responsible for inducing the toxic activity. *Ec*LPS containing a hexa-acylated lipid A portion binds to caspase-4/11 and induces the oligomerization of caspase-4/11 (7). Similarly, the synthetic compound 506 of *E. coli*-type hexa-acylated lipid A (lipid A-506) (15), induced an almost identical BRET saturation curve (open triangles in Fig. 2). In contrast, muramyl dipeptide (MDP) of Gram-positive bacteria cell walls, a negative control against LPS-binding proteins, did not induce the BRET signal (open circles in Fig. 2). These findings suggest that cytoplasmic *Ec*LPS induces the complex formation between rCasp11(C/A)-Rluc and rCasp11(C/A)-Venus with a specific stoichiometry.

BRET Assays for the Mutants of the LPS-binding Site of Caspase-4/11 – Caspase-4/11 recognizes LPS through the N-terminal CARD domain and Lys^{19} within the domain is essential for the interaction with LPS (7). The Lys^{19} residue is conserved in the corresponding CARD domain in caspase-4/11. We therefore designed constructs of the two sets of donor/acceptor recombinant proteins with an additional replacement of Lys^{19} with Glu^{19} in the CARD domain of caspase-4/11, rCasp11(C/A + K/E)-Rluc and rCasp11(C/A + K/E)-Venus or rCasp4(C/A + K/E)-Rluc and rCasp4(C/A + K/E)-Venus, to prevent the LPS binding activity of caspase-4/11. HEK293S GnTI$^-$ cells stably co-expressing the pair of fusion proteins rCasp11(C/A + K/E)-Rluc and rCasp11(C/A + K/E)-Venus exhibited no significant signal for the BRET saturation assay after electroporation of *Ec*LPS (closed circles in Fig. 3A), compared to the LPS-dependent hyperbolic BRET signal for those

expressing the pair of fusion proteins rCasp11(C/A)-Rluc and rCasp11(C/A)-Venus (open circles in Fig. 3A). Similarly, no significant BRET signal was observed for the pair of fusion proteins rCasp4(C/A + K/E)-Rluc and rCasp4(C/A + K/E)-Venus (Fig. 3B). Western blotting showed that the intracellular protein amounts for rCasp11(C/A + K/E)-Rluc and rCasp11(C/A + K/E)-Venus or rCasp4(C/A + K/E)-Rluc and rCasp4(C/A + K/E)-Venus were similar to those of rCasp11(C/A)-Rluc and rCasp11(C/A)-Venus or rCasp4(C/A)-Rluc and rCasp4(C/A)-Venus, respectively (Fig. 3C). These findings obtained by the BRET assays clearly indicated that the Lys^{19} residue in the CARD domain of caspase-4/11 is essential for the *Ec*LPS-dependent complex formation, and also indicate that the addition of either fusing tag to rCasp4/11 did not affect their LPS-binding activity.

Validation of Complex Formation with High-molecular Weight Oligomers of Caspase-4 on Cytoplasmic LPS – Shi *et al.* found an interesting phenomenon that rCasp4/11 expressed in insect cells elute at a size of ~100 kDa, corresponding to a monomer from a gel filtration column; whereas those expressed in *E. coli* are high-molecular weight oligomers of ~600 kDa (7). To verify whether the complex formation between caspase-4/11 molecules on LPS in living cells observed by the BRET assays contains not only dimers but also higher molecular-weight oligomers, we carried out a bimolecular fluorescent complementation (BiFC) assay combined with the BRET system. We designed two constructs, rCasp4(C/A)-Venus(N) and rCasp4(C/A)-Venus(C), containing either the N-terminal half or C-terminal half of the Venus tag. HEK293S GnTI$^-$ cells stably co-expressing

rCasp4(C/A)-Venus(N) and rCasp4(C/A)-Venus(C) produced similar positive fluorescent signals at the excitation wave length of 530 nm in an *Ec*LPS electroporation-dependent manner (closed circles in Fig. 4A), indicating that the co-expression of both constructs containing the Venus(N) and Venus(C) tags causes the functional reconstitution to complement the fluorescent signal equivalent to the intact Venus tag in the living cells. Interestingly, a positive BiFC-BRET saturation curve was not observed between the complemented Venus of the fusion proteins and rCasp4(C/A)-Rluc (closed circles in Fig. 4B).

Detection of Complex Formation of Caspase-4/11 on Penta-acylated LPS by BRET Assays – LPS prepared from *Rhodobacter sphaeroides* (*Rs*LPS) with penta-acylated lipid A is a potent antagonist for LPS-induced toxic shock in mice (4). To examine specific LPS-dependent complex formation of caspase-11, *Rs*LPS was transfected into HEK293S GnTI$^-$ cells stably expressing rCasp11(C/A)-Rluc and rCasp11(C/A)-Venus. Interestingly, *Rs*LPS induced a similar hyperbolic BRET saturation curve but the plateau was reduced to about 50% compared to that induced by *Ec*LPS (closed circles in Fig. 5A). Similar results of *Rs*LPS-dependent complex formation of caspase-4 were obtained using HEK293S GnTI$^-$ cells stably co-expressing rCasp4(C/A)-Rluc and rCasp4(C/A)-Venus (Fig. 5B).

DISCUSSION

The findings of the present study demonstrated specific LPS-dependent protein-protein interactions between rCasp4/11, rCasp4/11(C/A) fused with an Rluc- or Venus- tag, through their CARD domain in the living cells, using BRET saturation assays (Figs. 2 and 3). The distance between the Rluc and Venus fusion tags approached within 10 nm by protein-protein interactions of rCasp4/11(C/A) on cytoplasmic LPS incorporated by electroporation (Fig. 6A). Interestingly, the BiFC-BRET saturation assay between the complemented rCasp4(C/A)-Venus and rCasp4(C/A)-Rluc showed no BRET signal (Fig. 4), suggesting that rCasp4(C/A) could form dimers but not higher molecular-weight oligomers, including trimers on cytoplasmic LPS (Fig. 6B) or that rCasp4(C/A) could form at least trimers, but the protein-protein interactions of the rCasp4(C/A) molecules in the complex caused an inappropriate orientation between the fusion tags of Rluc and Venus, preventing BRET (Fig. 6C).

*Rs*LPS is an antagonist of caspase-4/11 and it binds caspase-4/11 but fails to induce their oligomerization (7). *Rs*LPS induced the BRET saturation curve, but *Rs*LPS reduced the BRET efficiency between rCasp4/11(C/A)-Rluc and rCasp4/11(C/A)-Venus by half compared to that of *Ec*LPS with the hexa-acylated lipid A (Fig. 5). These findings indicate that the oligomers of rCasp4/11(C/A) on cytoplasmic *Rs*LPS do not have sufficient protein-protein interactions to induce

the highly efficient BRET signal obtained by *Ec*LPS (Fig. 6D), and also demonstrate that the homotypic complex formation of caspase-4/11 on cytoplasmic *Rs*LPS does not induce their autocatalytic activation to trigger pyroptosis of the cells infected with *R. sphaeroides.*

The horseshoe crab *T. tridentatus* factor C, an LPS-sensitive serine protease zymogen, is autocatalytically activated to α-factor C on the surface of LPS through the N-terminal Cys-rich region of the molecule containing the tripeptide sequence -Arg^{36}-Trp^{37}-Arg^{38}- (12). Moreover, the distance between Arg^{1} and the tripartite sequence of the LPS-binding site are essential elements for the autocatalytic activation of factor C (13), suggesting that the N-terminal Arg^{1} is essential for inducing specific protein-protein interactions between factor C molecules in close proximity and with the proper orientation on the surface of LPS, leading to autocatalytic activation (13). Similarly, the Lys^{19} residue of caspase-4/11 in the CARD domain was also confirmed to be an essential residue for binding LPS (Figs. 3A and 3B). In addition to the Lys^{19} residue, the tripartite sequence -Lys^{52}-Arg^{53}-Trp^{54}- of the CARD domain in caspase-11 is an essential element for its LPS-binding activity (7). Interestingly, the distance between the Lys^{19} residue and the tripartite sequence of caspase-11 was almost the same as that between the essential elements required for the autocatalytic activation of factor C. Therefore, the N-terminal region containing the basic residues of the LPS-responsive protease zymogens, factor C and caspase-11, may play important roles for the proper orientation of their oligomers on the surface of LPS to lead to autocatalytic activation.

Recently, we found that factor B, a substrate of α-factor C, is the second LPS-binding protease zymogen in the LPS-induced coagulation cascade, and that the N-terminal clip domain of factor B has an important role in localizing factor B to the surface of bacterial LPS to initiate effective proteolytic activation by α-factor C (16). Gasdermin D is an intracellular protein substrate for caspase-11 and the resulting N-terminal domain binds membrane lipids, phosphoinositides, and cardiolipin to produce membrane-disrupting cytotoxicity in mammalian cells and artificially transformed bacteria (17). It is unclear whether gasdermin D can bind to LPS; cytoplasmic LPS may enhance the proteolytic cleavage of gasdermin D by caspase-11 activated on LPS.

Ligands other than LPS were recently found to have important roles in the activation of caspase-4/11: caspase-11 binds endogenous oxidized phospholipids to induce IL-1β release from living dendritic cells without triggering pyroptosis (18) and saturated fatty acids, including palmitate, activate caspase-4 in monocytes, triggering IL-1β release (19). The BRET saturation analysis as shown in this study provides new insight for the interaction of caspase-4/11 with these new ligands.

EXPERIMENTAL PROCEDURES

Materials – The HEK293 mutant cell line (HEK293S GnTI$^-$) was obtained from ATCC. *Ec*LPS and MDP were purchased from Sigma-Aldrich (St. Louis, MO) and used to measure dead cells with a cell imager and BRET saturation assays. Synthetic lipid A (lipid A-506) was purchased from Peptide Institute Inc. (Osaka, Japan) and *Rs*LPS was purchased from InVivoGen (Waltham, MA). Coelenterazine H was purchased from Promega (Madison, WI) and used for a luminescent reaction substrate of Rluc. Polyclonal antibodies against caspase-4 and caspase-11 were purchased from Santa Cruz Biotechnology (Dallas, TX). Anti-α-tubulin pAb-HRP-DirecT antibody was purchased from MBL (Nagoya, Japan). Calcein-AM and DAPI were purchased from Dojindo Laboratories (Kumamoto, Japan).

Cloning and Mutagenesis – The full-length DNA fragment of caspase-11 was amplified by PCR from mouse fibroblast cells and subcloned into pcDNA3.1 (−) and pCEP4 vectors. Venus and Rluc tags were inserted into the C-terminus of rCasp11 or rCasp11(C/A) in pcDNA3.1 (−) and pCEP4, respectively. The full-length DNA fragment of caspase-4 was obtained from GenScript (Piscataway, NJ) and pcDNA3.1 (−) and pCEP4 vectors containing caspase-4 cDNA was constructed using the same methods as for caspase-11. DNA mutations were introduced using site-directed mutagenesis by inverse PCR. For BiFC-BRET, rCasp4(C/A) fused with the N-terminal truncated version of Venus (1-

154 amino acid) or the C-terminal truncated version of Venus (155-231 amino acid) at the C-terminal caspase-4 was inserted into the pIRES vector for bicistronic expression.

Establishment of Stable Cell Lines – To establish HEK293S GnTI$^-$ cells stably expressing the recombinant protein of rCasp4/11, cells transfected with 0.25-0.5 μg of the corresponding plasmids by electroporation were plated on a 6-cm dish (1.1×10^5 cells). After 20 h, the medium in the dish was replaced with DMEM containing 0.9 mg/ml G418 and 0.5 mg/ml hygromycin (Nacalai Tesque, Kyoto, Japan) for cell selection. One week later, the selected cells were isolated.

BRET Saturation Assay – BRET assays were performed as described previously (20). All the BRET signals were measured using a FlexStation 3 Microplate Reader (Molecular Devices, Sunnyvale, CA) at 37°C. For the assays, HEK293S GnTI$^-$ cells transfected with *Ec*LPS, *Rs*LPS, lipid A-506, or MDP by electroporation were plated on 12-well plates (2.5×10^5 cells/well). Transfection of these substances into cells was performed using the Neon Transfection System (Life Technologies, Carlsbad, CA) following the manufacturer's instructions. One-hour post-transfection, the cells were washed once with 10 mM PBS (pH 7.2) and collected by centrifugation ($800 \times g$ for 5 min). The cell pellets were then resuspended in 80 μl Dulbecco's PBS (pH 7.2), and two 40-μl aliquots of the cell suspensions were transferred to each well of white 96-well microplates (duplicate wells). After adding 10 μl of Rluc substrate (Coelenterazine H, 25 μM) into each sample, followed by 30 s of gentle mixing,

luminescence was measured simultaneously for the donor (λ_{em} = 475 nm; short wavelength) and acceptor (λ_{em} = 530 nm; long wavelength). Saturation data analysis was performed using the following equation, as described previously (20): BRET signal = [long wavelength] / [short wavelength] − [long wavelength] $_{\text{donor only}}$ / [short wavelength] $_{\text{donor only}}$. BRET signals were shown as relative values to that when the cells were electroporated with *Ec*LPS at 0.57 μg/ml.

Western Blotting – Samples were subjected to SDS-PAGE in a 12% slab gel and transferred to a PVDF membrane. After blocking with 5% skim milk, the membrane was incubated with polyclonal antibodies against caspase-4/11, after which it was incubated with the secondary antibody (HRP-conjugated goat anti-mouse IgG or anti-rabbit IgG, Bio-Rad, Hercules, CA), or incubated with anti-α-tubulin pAb-HRP-DirecT, followed by development with WesternBright Quantum (Advansta, Menlo Park, CA). Precision Plus Protein Dual Color standards (**Bio-Rad**) were used to determine apparent molecular masses.

Fluorescence Imaging – HEK293S GnTI$^-$ cells stably expressing the recombinant proteins were transfected with 1 μg *Ec*LPS or other substances and plated on 6-well plates (2.5×10^5 cells/well). One-hour post-transfection, living and dead cells were detected with Calcein-AM and DAPI, respectively. All the cells were imaged using the ZOE Fluorescent Cell Imager (Bio-Rad).

REFERENCES

1. Zhao, Y., and Shao, F. (2016) Diverse mechanisms for inflammasome sensing of cytosolic bacteria and bacterial virulence. *Curr. Opin. Microbiol.* **29,** 37–42

2. Man, S. M., and Kanneganti, T. D. (2015) Regulation of inflammasome activation. *Immunol. Rev.* **265,** 6–21

3. Yang, C. S., Shin, D. M., and Jo, E. K. (2012) The role of NLR-related protein 3 inflammasome in host defense and inflammatory diseases. *Int. Neurourol. J.* **16,** 2-12

4. Kayagaki, N., Warming, S., Lamkanfi, M., Vande Walle, L., Louie, S., Dong, J., Newton, K., Qu, Y., Liu, J., Heldens, S., Zhang, J., Lee, W. P., Roose-Girma, M., and Dixit, V. M. (2011) Non-canonical inflammasome activation targets caspase-11. *Nature* **479,** 117–121

5. Kayagaki, N., Wong, M. T., Stowe, I. B., Ramani, S. R., Gonzalez, L. C., Akashi-Takamura, S., Miyake, K., Zhang, J., Lee, W. P., Muszyński, A., Forsberg, L. S., Carlson, R. W., and Dixit, V. M. (2013) Noncanonical inflammasome activation by intracellular LPS independent of TLR4. *Science* **341,** 1246–1249

6. Hagar, J. A., Powell, D. A., Aachoui, Y., Ernst, R. K., and Miao, E. A. (2013) Cytoplasmic LPS activates caspase-11: implications in TLR4-independent endotoxic shock. *Science* **341** 1250-1253

7. Shi, J., Zhao, Y., Wang, Y., Gao, W., Ding, J., Li, P., Hu, L., and Shao, F. (2014) Inflammatory caspases are innate immune receptors for intracellular LPS. *Nature* **514,** 187-192

8. Muta, T., Miyata, T., Misumi, Y., Tokunaga, F., Nakamura, T., Toh, Y., Ikehara, Y., and Iwanaga, S. (1991) Limulus factor C. An endotoxin-sensitive serine protease zymogen with a mosaic structure of complement-like, epidermal growth factor-like, and lectin-like domains. *J. Biol. Chem.* **266**, 6554-6561

9. Ariki, S., Takahara, S., Shibata, T., Fukuoka, T., Ozaki, A., Endo, Y., Fujita, T., Koshiba, T., and Kawabata, S. (2008) Factor C acts as a lipopolysaccharide-responsive C3 convertase in horseshoe crab complement activation. *J. Immunol.* **181,** 7994–8001

10. Tagawa, K., Yoshihara, T., Shibata, T., Kitazaki, K., Endo, Y., Fujita, T., Koshiba, T., and Kawabata, S. (2012) Microbe-specific C3b deposition in the horseshoe crab complement system in a C2/factor B-dependent or -independent manner. *PLoS One* **7,** e36783

11. Ariki, S., Koori, K., Osaki, T., Motoyama, K., Inamori, K., and Kawabata, S. (2004) A serine protease zymogen functions as a pattern-recognition receptor for lipopolysaccharides. *Proc. Natl. Acad. Sci. USA.* **101**, 953-958

12. Koshiba, T., Hashii, T., and Kawabata, S. (2007) A structural perspective on the interaction between lipopolysaccharide and factor C, a receptor involved in recognition of Gram-negative bacteria. *J. Biol. Chem.* **282,** 3962–3967

13. Kobayashi, Y., Shiga, T., Shibata, T., Sako, M., Maenaka, K., Koshiba, T., Mizumura, H., Oda, T., and Kawabata, S. (2014) The N-terminal Arg residue is essential for autocatalytic activation of a lipopolysaccharide-responsive protease zymogen. *J. Biol. Chem.* **289,** 25987–25995

14. Pfleger, K. D. G., Seeber, R. M., and Eidne, K. A. (2006) Bioluminescence resonance energy transfer (BRET) for the real-time detection of protein-protein interactions. *Nat. Protoc.* **1,** 337–345

15. Imoto, M., Kusumoto, S., Shiba, T., Rietschel, E.Th., Galanos, C., and Lüderitz, O. (1985) Chemical structure of Escherichia coli lipid A. Tetrahedron *Lett.* 26, 907-908

16. Kobayashi, Y., Takahashi, T., Shibata, T., Ikeda, S., Koshiba, T., Mizumura, H., Oda, T., and Kawabata, S. (2015) Factor B is the second lipopolysaccharide-binding protease zymogen in the horseshoe crab coagulation cascade. *J. Biol. Chem.* **290,** 19379–19386

17. Ding, J., Wang, K., Liu, W., She, Y., Sun, Q., Shi, J., Sun, H., Wang, D. C., and Shao, F. (2016) Pore-forming activity and structural autoinhibition of the gasdermin family. *Nature* **535,** 111–116

18. Zanoni, I., Tan, Y., Di Gioia M., Broggi, A., Ruan, J., Shi, J., Donado, C. A., Shao, F., Wu, H., Springstead, J. R., and Kagan, J. C. (2016) An endogenous caspase-11 ligand elicits interleukin-1 release from living dendritic cells. *Science* **352,** 1232–1236

19. Pillon, N. J., Chan, K. L., Zhang, S., Mejdani, M., Jacobson, M. R., Ducos, A., Bilan, P. J., Niu, W., and Klip, A. (2016) Saturated fatty acids activate caspase-4/-5 in human monocytes, triggering IL1β and IL18 release. *Am. J. Physiol. Endocrinol. Metab.* **311,** 825-835

20. Sasaki, O., Yoshizumi, T., Kuboyama, M., Ishihara, T., Suzuki, E., Kawabata, S., and Koshiba, T. (2013) A structural perspective of the MAVS-regulatory mechanism on the mitochondrial outer membrane using bioluminescence resonance energy transfer. *Biochim. Biophys. Acta* **1833,** 1017–1027

FIGURE LEGENDS

Fig. 1. Viability of HEK293S GnTI$^-$ cells stably expressing rCasp11 or co-expressing rCasp11-Rluc and rCasp11-Venus. (A) HEK293S GnTI$^-$ cells stably expressing rCasp11 or co-expressing rCasp11-Rluc and rCasp11-Venus were transfected with (+) or without (–) 1 μg *Ec*LPS by electroporation. (B) Percentage of DAPI positive cells was calculated with 200~230 cells per field under each condition. Values shown are means ± SEM (n = 3). ***P<0.001.

Fig. 2. Complex formation of rCasp11(C/A)-Rluc and rCasp11(C/A)-Venus on cytoplasmic LPS by BRET saturation assays. HEK293S GnTI$^-$ cells stably co-expressing rCasp11(C/A)-Rluc and rCasp11(C/A)-Venus were transfected with increasing concentrations of *Ec*LPS, lipid A-506, or MDP. ●, *Ec*LPS; ○, MDP; ▲, no ligand; △, lipid A-506. Values shown are means ± SEM (n = 3).

Fig. 3. Validation of LPS-binding site of caspase-4/11 by BRET saturation assays. (A) HEK293S GnTI$^-$ cells stably co-expressing rCasp11(C/A)-Rluc and rCasp11(C/A)-Venus or rCasp11(C/A + K/E)-Rluc and rCasp11(C/A + K/E)-Venus were transfected with the increasing concentrations of *Ec*LPS. Values shown are means ± SEM (n = 3). ●, rCasp11(C/A + K/E); ○,

rCasp11(C/A). (B) The same experiments as in (A) using the HEK293S GnTI$^-$ cells stably co-expressing rCasp4(C/A) and rCasp4(C/A + K/E). ●, rCasp4(C/A + K/E); ○, rCasp4(C/A). (C) Cell extracts from the HEK293S GnTI$^-$ cells in (A) and (B) were subjected to Western blotting with the indicated antibodies. Anti-tubulin was used as the loading control for each sample.

Fig. 4. Validation of high-molecular weight oligomer formation of rCasp4 on *Ec*LPS by BiFC-BRET saturation assays. (A) HEK293S GnTI$^-$ cells stably co-expressing rCasp4(C/A)-Rluc and rCasp4(C/A)-Venus or rCasp4(C/A)-Rluc and rCasp4(C/A)-Venus(N) and rCasp4(C/A)-Venus(C) were transfected with the increasing concentrations of *Ec*LPS. Values shown are means ± SEM (n = 3). ●, complemented Venus; ○, full length Venus. (B) BiFC-BRET saturation assays of the same cells as (A). Values shown are means ± SEM (n = 3). ●, complemented Venus; ○, full length Venus.

Fig. 5. Detection of complex formation of rCasp4/11 on *Rs*LPS by BRET saturation assays. (A) HEK293S GnTI$^-$ cells stably co-expressing rCasp11(C/A)-Rluc and rCasp11(C/A)-Venus were transfected with the increasing concentrations of *Rs*LPS or *Ec*LPS. ●, *Rs*LPS; ○, *Ec*LPS. Values shown are means ± SEM (n = 3). (B) The same experiments as in (A) using HEK293S

GnTI$^-$ cells stably co-expressing rCasp4(C/A)-Rluc and rCasp4(C/A)-Venus. ●, *Rs*LPS; ○, *Ec*LPS.

Fig. 6. Schematic models of homotypic interaction of rCasp4/11 fused with Rluc and Venus or complemented Venus tags on *Ec*LPS or *Rs*LPS.

(A) rCasp4/11 forms a homotypic dimer on *Ec*LPS to induce sufficient BRET between the Rluc and Venus tags. (B) rCasp4/11 cannot form higher oligomers, including a trimer, on *Ec*LPS, which does not induce BRET between the Rluc and complemented Venus tags. (C) rCasp4/11 forms at least a homotypic trimer on *Ec*LPS, but the trimeric complex formation causes an inappropriate orientation between the Rluc and complemented Venus tags, which does not induce BRET. (D) Homotypic dimerization of rCasp4/11 on penta-acylated *Rs*LPS causes an inappropriate orientation between the Rluc and Venus tags, which reduces the BRET efficiency.

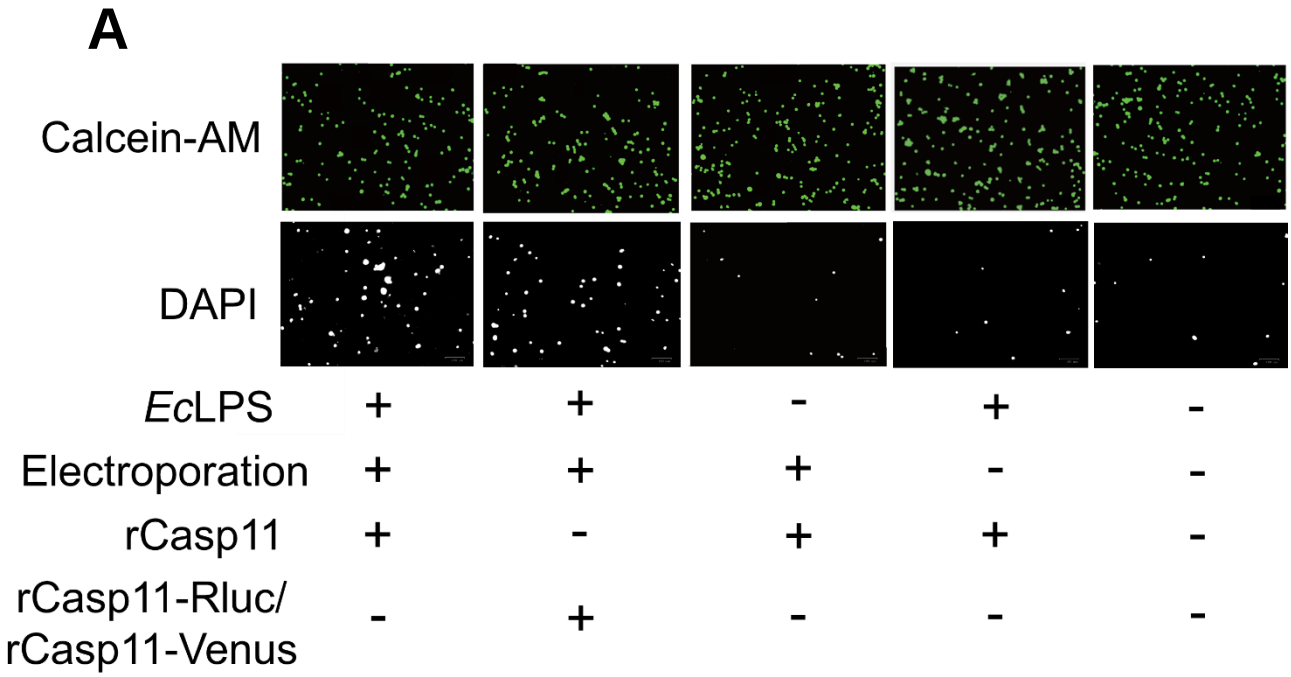
A
Calcein-AM
DAPI
EcLPS + + - + -
Electroporation + + + - -
rCasp11 + - + + -
rCasp11-Rluc/
rCasp11-Venus - + - - -

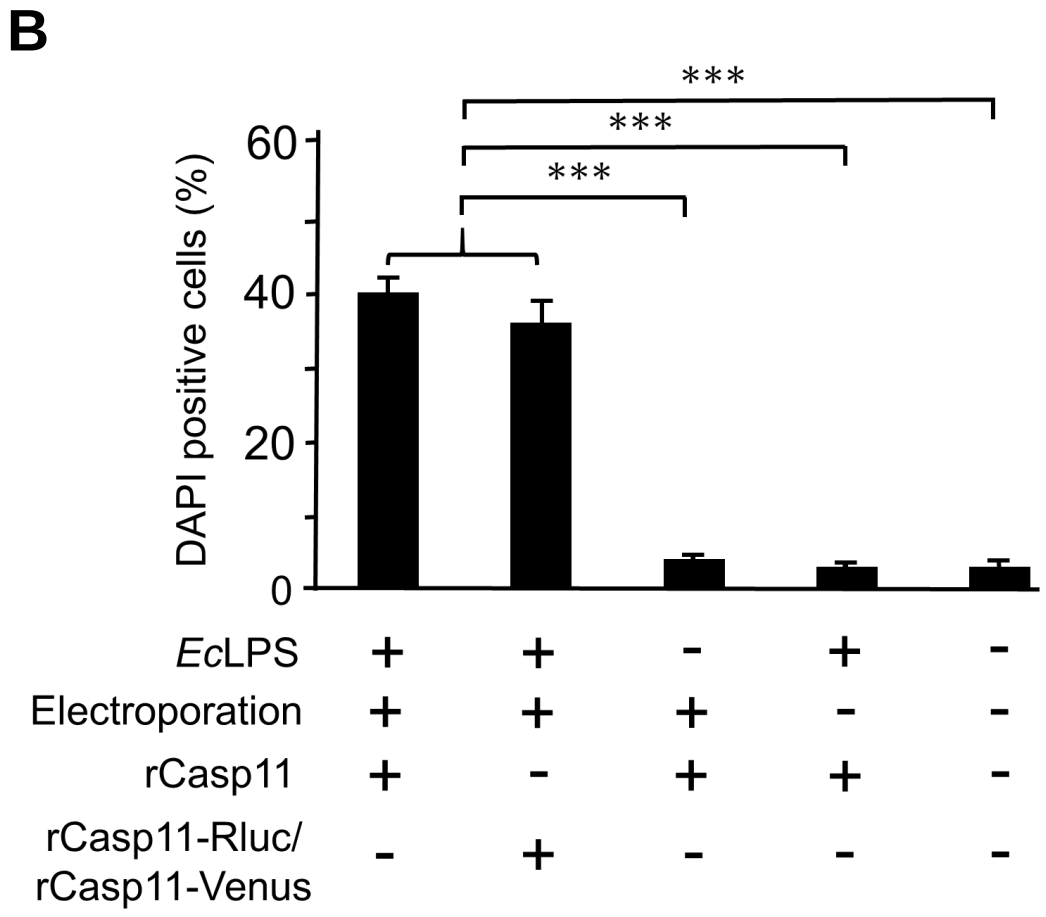
B
***
***
***
DAPI positive cells (%)
60
40
20
0
EcLPS + + - + -
Electroporation + + + - -
rCasp11 + - + + -
rCasp11-Rluc/
rCasp11-Venus - + - - -

Figure 1

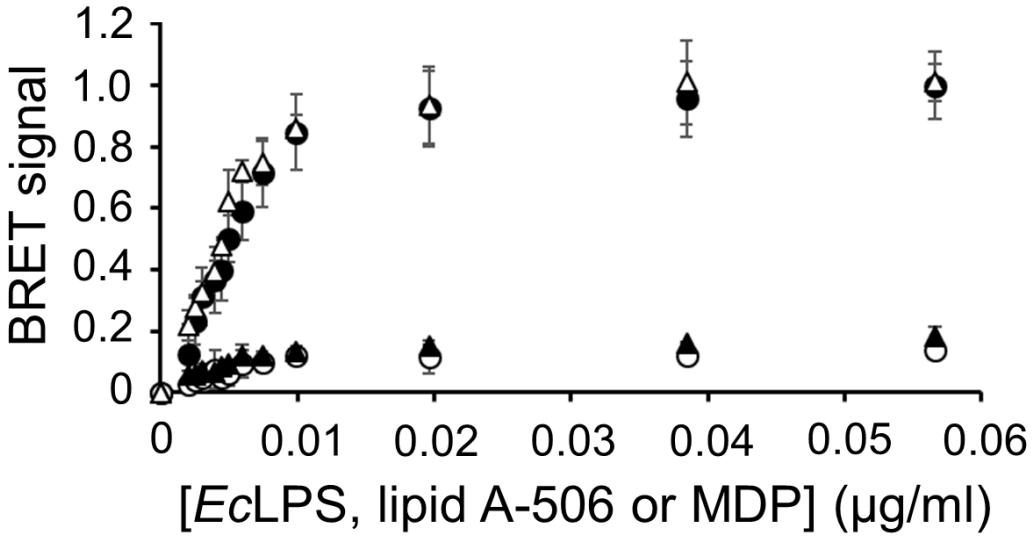
BRET signal
1.2
1.0
0.8
0.6
0.4
0.2
0
0
0.01
0.02
0.03
0.04
0.05
0.06
[*Ec*LPS, lipid A-506 or MDP] (µg/ml)

Figure 2

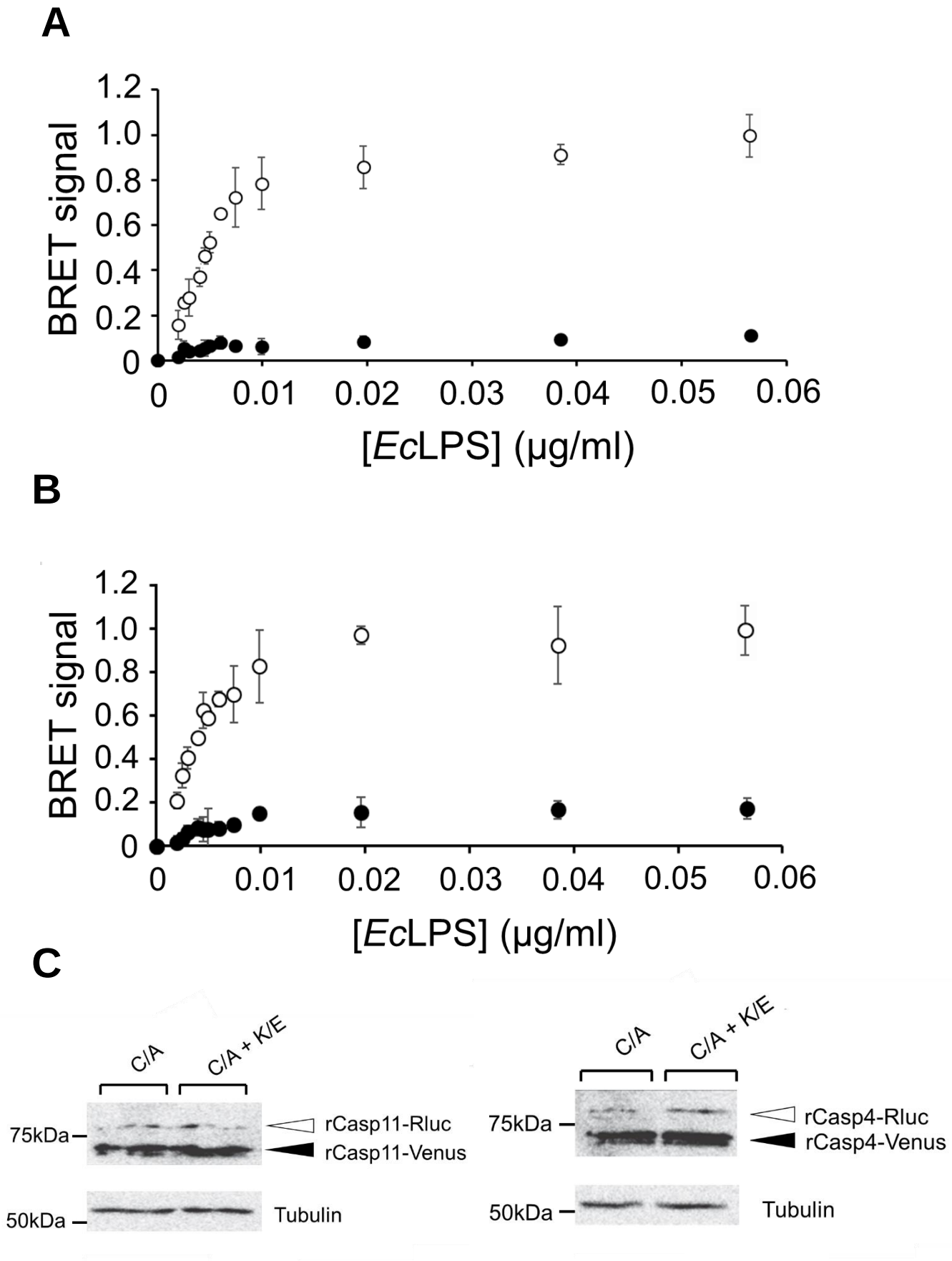
A
BRET signal
1.2
1.0
0.8
0.6
0.4
0.2
0
0
0.01
0.02
0.03
0.04
0.05
0.06
[EcLPS] (µg/ml)
B
BRET signal
1.2
1.0
0.8
0.6
0.4
0.2
0
0
0.01
0.02
0.03
0.04
0.05
0.06
[EcLPS] (µg/ml)
C
C/A
C/A + K/E
75kDa
rCasp11-Rluc
rCasp11-Venus
50kDa
Tubulin
C/A
C/A + K/E
75kDa
rCasp4-Rluc
rCasp4-Venus
50kDa
Tubulin

Figure 3

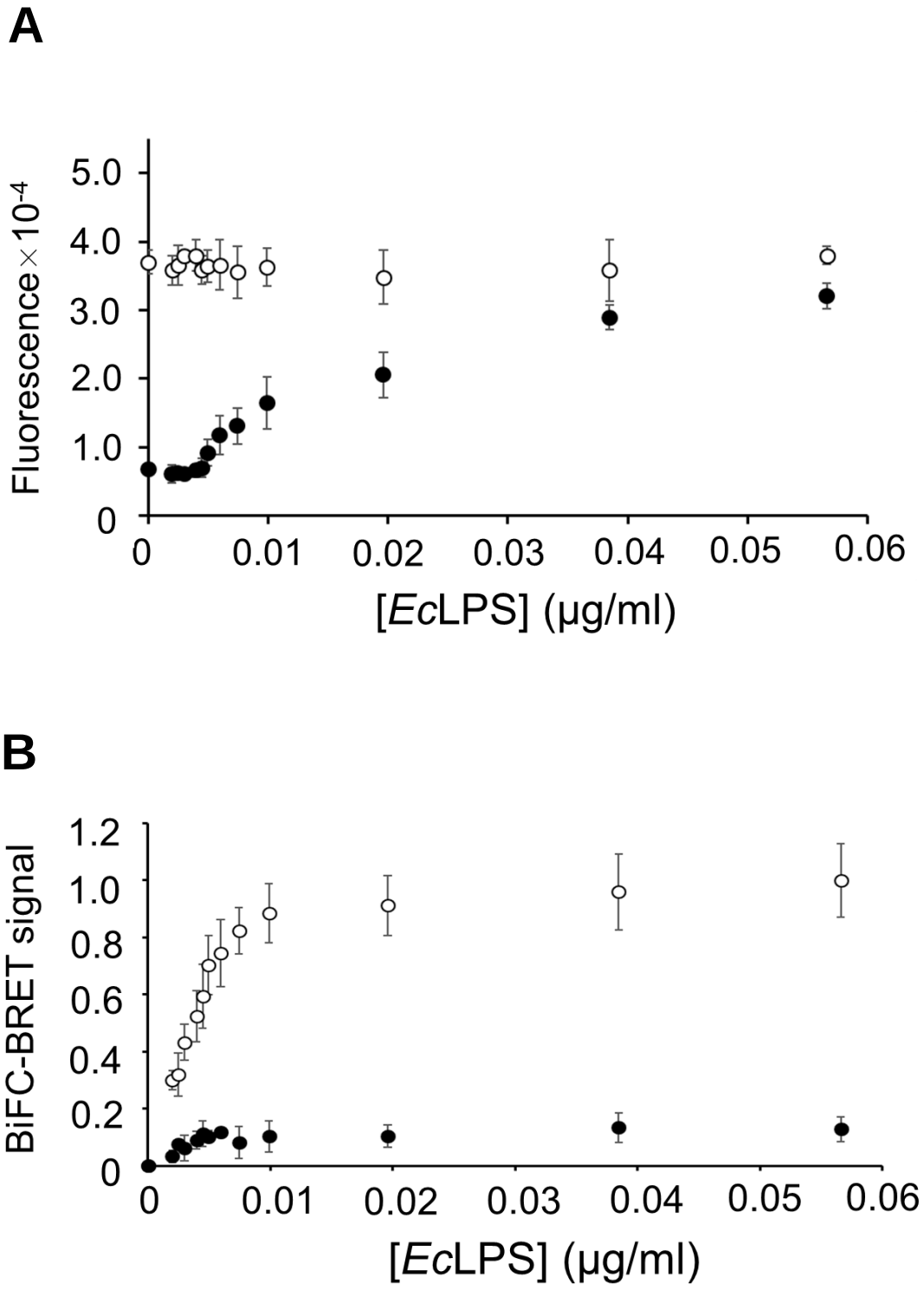
A
Fluorescence×10-4
5.0
4.0
3.0
2.0
1.0
0
0
0.01
0.02
0.03
0.04
0.05
0.06
[EcLPS] (μg/ml)
B
BiFC-BRET signal
1.2
1.0
0.8
0.6
0.4
0.2
0
0
0.01
0.02
0.03
0.04
0.05
0.06
[EcLPS] (μg/ml)

Figure 4

A

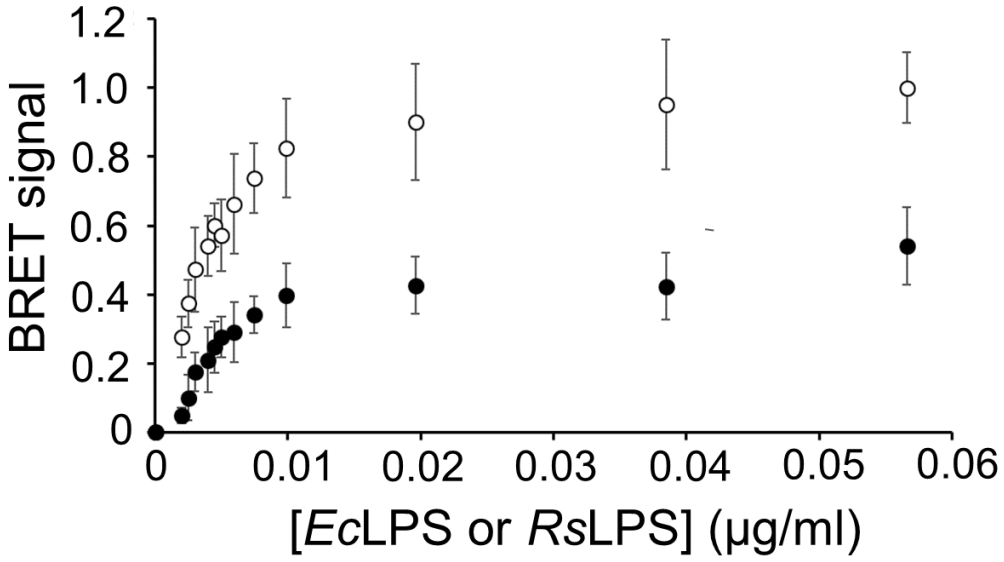
BRET signal
1.2
1.0
0.8
0.6
0.4
0.2
0
0
0.01
0.02
0.03
0.04
0.05
0.06
[*Ec*LPS or *Rs*LPS] (µg/ml)

B

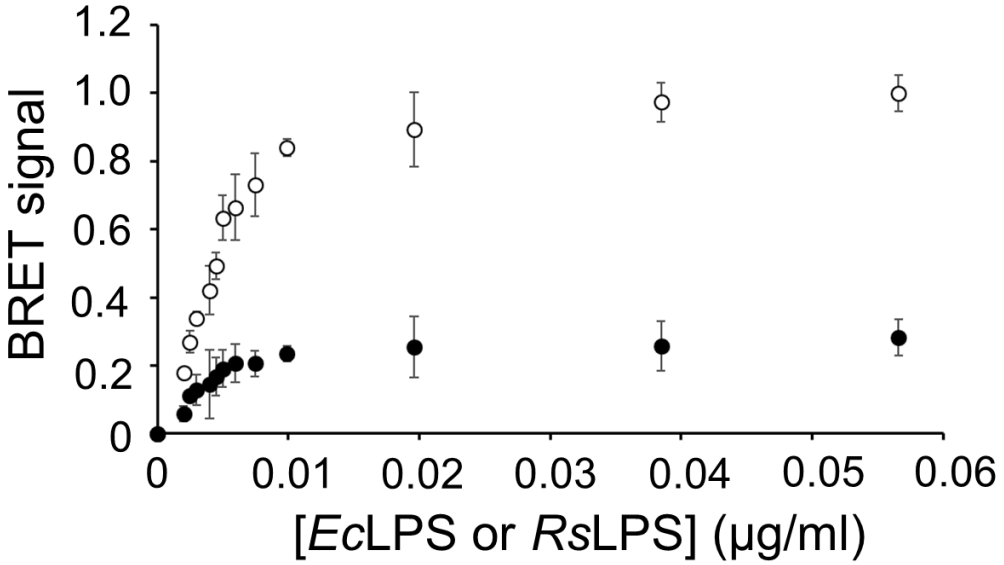
BRET signal
1.2
1.0
0.8
0.6
0.4
0.2
0
0
0.01
0.02
0.03
0.04
0.05
0.06
[*Ec*LPS or *Rs*LPS] (µg/ml)

Figure 5

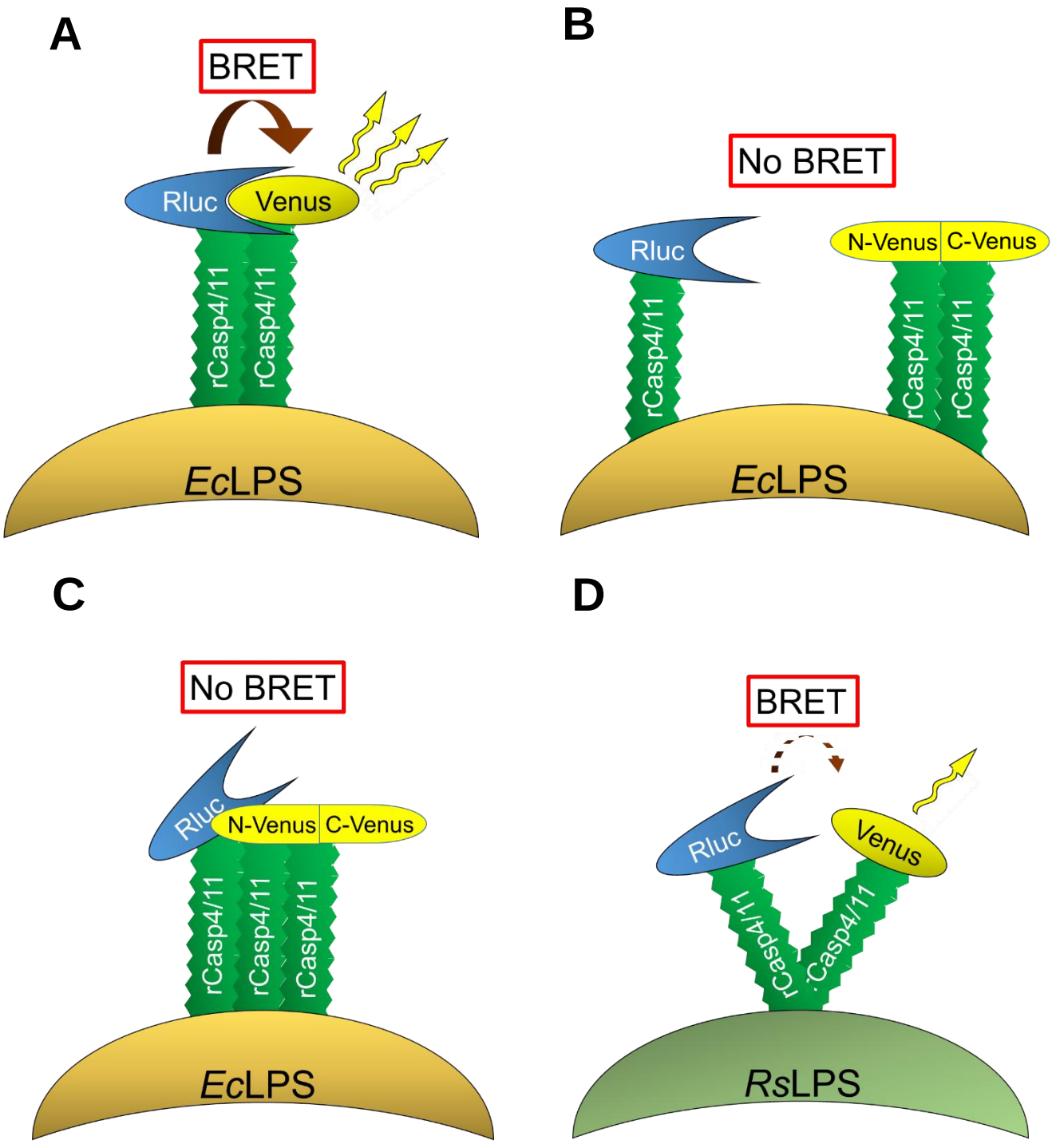
A
BRET
Rluc
Venus
rCasp4/11
rCasp4/11
EcLPS
B
No BRET
Rluc
N-Venus
C-Venus
rCasp4/11
rCasp4/11
rCasp4/11
EcLPS
C
No BRET
Rluc
N-Venus
C-Venus
rCasp4/11
rCasp4/11
rCasp4/11
EcLPS
D
BRET
Rluc
Venus
rCasp4/11
rCasp4/11
RsLPS

Figure 6

ACKNOWLEDGEMENTS

Studies described in this thesis had been carried out under the cordial guidance of professor Shun-ichiro Kawabata (Kyushu University). I am grateful to Dr. Yuki Kobayashi (Kyushu University), Dr. Toshio Shibata (Kyushu University), Dr. Takumi Koshiba (Kyushu University) for their helpful discussions and suggestions. I also acknowledge Dr. Yoshiharu Matsuura (Osaka University) for providing the HA-tagged NS3/4A and Dr. Katsuyoshi Mihara (Kyushu University) for kindly supplying the rat Tom-22 and mouse Omp-25 expression plasmids. I greatly appreciate Dr. Atsushi Miyawaki (RIKEN) for providing the Venus cDNA and Dr. Stephen Girardin (University of Toronto) for providing the NLRX1 poly-clonal antibody. I also appreciate Ms. Yuko Fuchigami for technical assistance with cloning and DNA sequencing, and Dr. Akane Oishi for technical assistance with electron microscopy and Mr. Nasir Bashiruddin (The University of Tokyo) for early work on this study. I would like to thank all the members of our laboratory for providing practical help and advices. Finally, I would like to give my personal thanks to my family and friends for continuing encouragement and understanding of this study.